# Master Laboratory

# $Z^0$-Resonance

## Group 18

Performed on March 22th–April 2nd
under supervision of

**Abstract**

This report is a study of various aspects of the standard model with a special focus on the $Z^0$ boson. Specifically, data from the OPAL experiment at CERN is used and analysed in a way similar to the historic experiment, but in a simplified fashion. Using Monte Carlo simulated data of the experiment, conditions were defined with which particular decay rates could be extracted from real experimental data. These rates could be recalculated into cross-sections for different beam energies at which Breit-Wigner functions were fitted. From this fits the $Z^0$ boson mass $M_Z = (91.19 \pm 0.05)\,\mathrm{GeV}$, its total decay width $\Gamma = (2.52 \pm 0.07)\,\mathrm{GeV}$ and its partial decay widths $\Gamma_e = (82 \pm 3)\,\mathrm{MeV}$, $\Gamma_\mu = (81 \pm 4)\,\mathrm{MeV}$, $\Gamma_\tau = (85 \pm 8)\,\mathrm{MeV}$, $\Gamma_h = (1820 \pm 70)\,\mathrm{MeV}$ were determined.

These results are quite reasonable and the current reference values given by the Particle Data Group [4] are within a 1-$\sigma$ environment for most of these results; the exception being the hadron decay width $\Gamma_h$, for which the reference value is within a 2-$\sigma$ environment.

By comparing different leptonic branching ratios, the lepton universality could be verified to a degree. Furthermore, the number of neutrino generations could be determined from the decay widths to a value of $N_\nu = 2.7 \pm 0.6$, which is a satisfying result and compatible with the expected value of 3.

At last, the forward-backward asymmetry of muons was determined and used to find an estimation of the squared sine of the Weinberg angle $\sin^2 \theta_W = 0.239 \pm 0.005$ which is again in good agreement with the reference value of the Particle Data Group.

# Contents

# 1. Introduction

Todays best known model to describe the physics of elementary particles is the Standard Model of particle physics. It describes three of the four known fundamental forces, that is, the electromagnetic force, the weak force and the strong force. The gravitational force, however, is not included in the Standard Model. With the finding of the Higgs boson in 2012 the last predicted particle of the Standard Model was found and also if there are physical effects which indicate that the standard model is not sufficient and extensions have to be made, it is still the most precise model to describe the interaction of elementary particles known.

In the 90s the OPAL (Omni Purpose Apparatus at LEP) experiment was operated at CERN. It was one of the major experiments at the Large Electron-Positron Collider (LEP). In the first half of the 90s the main goal of the experiment was to investigate the $Z^0$ boson, calculating its mass and decay width precisely for example. In the second half, after the expansion of the LEP which lead to the possibility of conducting experiments with much higher center of mass energies, the investigation focused mainly on $W^{\pm}$boson pairs.

In this report we present an analysis of OPAL data from the early 90s. Following the analysis done back than in a simplified way, with the goal to calculate the $Z^0$ mass, decay width, its partial decay widths, the number of neutrino generations, an estimation of the squared sine of the Weinberg angle using the forward-backward asymmetry of muons and verify the lepton universality.

The experiment can roughly be divided into two parts. In the first part, the event display GROPE will be used to visualize the characteristic detector signals of the different particles. Based on the properties of these signals, we devise selection criteria to differentiate between different event types. In the second part, Monte Carlo (MC) data simulating the actual OPAL data will be used to further refine these cuts in the detector data. After that, these selection criteria will be applied to the OPAL data, such that the wanted variables can be computed using a statistical analysis.

The report itself is structured as follows. In section 2, a short overview for the needed theoretical background is given. Further, structure and function of the detector is presented and the characteristics of the different particles will be discussed. Afterwards in section 3 this is followed by the description and presentation of the analysis. At the end we summarize and discuss the results of the analysis in section 4.

2

## 2. Theory

### 2.1. The Standard Model

In the Standard Model the interaction between particles is described by the three fundamental interactions: electromagnetic, weak and strong interaction. The fourth fundamental interaction that we know of, gravitation, is not described by the Standard Model, but is also to weak to play any role regarding experiments with single particles.

Each of this interactions or forces has different mediator particles, which all are bosons (integer spin particles) which classifies one of two groups of elementary particles in the Standard Model. The second group are the fermions (half-integer spin particles), which can be divided in further subgroups. For the electromagnetic interaction the mediator particle is the photon ($\gamma$) which couples to the electric charge of particles. For the weak interaction there exist three mediator particles, namely the $W^+$, $W^-$ and $Z^0$ bosons. The weak bosons couple to the weak isospin. So called gluons ($g$) are the mediator bosons for the strong interaction they connect to the color charge. The last boson of the Standard Model is the higgs boson ($H^0$), the only boson of the Standard Model with spin zero (the other one named have spin one). It is the latest discovered particle of the Standard Model and is needed for the mass generation of the other vector bosons via spontaneous symmetry breaking. An overview over the vector bosons is given in table 1.

The fermions can be divided in three generations of quarks and leptons. Quarks are the fundamental particles out of which hadrons are build and for each generation one pair of quark exists. The leptons can be divided further into charged and non charged leptons which refers to the electric charge of the particles. The non charged leptons are called neutrinos and in total there are three neutrinos, one for each generation. There are also three charged leptons: electron, muon and tau. An overview over the fermions is given in table 2.

A more in-depth presentation of the Standard Model of particle physics is given in the book of Povh [6]. A more casual introduction can be found in the reference [8].

In the following paragraphs we will especially focus on the creation of $Z^0$ boson via electron-positron scattering.

Table 1: An overview over the bosonic particles of the Standard Model. Based on the book of Povh [6].

| Interaction | Vector Boson | El. Charge [$e$] | Mass [GeV/$c_0^2$] |
|---|---|---|---|
| Electromagnetic | $\gamma$ : Photon | 0 | 0 |
| Weak | $W^\pm$: $W^\pm$-boson | $\pm 1$ | 80.399 |
| | $Z^0$: $Z^0$-boson | 0 | 91.188 |
| Strong | $g$: Gluons | 0 | 0 |

Table 2: An overview over the elementary fermionic particles of the Standard Model. Based on the book of Povh [6].

| Group | Generation | Flavour | El. charge [$e$] | Mass [MeV/$c_0^2$] |
|---|---|---|---|---|
| Leptons (Spin-$\frac{1}{2}$) | First | $e$: Electron | $-1$ | 0.511 |
| | | $\nu_e$: Electron neutrino | 0 | < 0.002 |
| | Second | $\mu$: Muon | $-1$ | 105.66 |
| | | $\nu_\mu$: Muon neutrino | 0 | < 0.19 |
| | Third | $\tau$: $\tau$-lepton | $-1$ | 1776.99 |
| | | $\nu_\tau$: $\tau$-lepton neutrino | 0 | < 0.18 |
| Quarks (Spin-$\frac{1}{2}$) | First | $u$: Up | 2/3 | 2.2 $^{+0.5}_{-0.4}$ |
| | | $d$: Down | $-1/3$ | 4.7 $^{+0.5}_{-0.3}$ |
| | Second | $c$: Charm | 2/3 | 1290 |
| | | $s$: Strange | $-1/3$ | 95 $^{+9}_{-3}$ |
| | Third | $t$: Top | 2/3 | 172 900 |
| | | $b$: Bottom | $-1/3$ | 4190 |

## 2.2. The $Z^0$ boson and $e^+e^-$-interactions

The process studied in this report is $e^+e^- \to f\bar{f}$ which in lowest order of perturbation theory is mediated by a photon or $Z^0$ boson. The Feynman diagrams for this processes are show in fig. 1. It should be mentioned that the top quark cannot be produced by decays of the $Z^0$ boson as the top quark's high mass makes this process kinematically impossible.

If the center-of-mass energy of the electron positron pair is near the $Z^0$ mass the s-channel decay is mostly mediated by the $Z^0$ boson, which can be seen as a peak of the cross-section.

One goal of the analysis in this report is to determine the total decay width and the partial decay widths, with the total decay width $\Gamma$ being given by the sum of the partial widths:

$$\Gamma = \Gamma_e + \Gamma_\mu + \Gamma_\tau + \Gamma_{\text{hadr.}} + \Gamma_\nu + \Gamma_{\text{unknown}}. \tag{1}$$

The Standard Model predicts a value of zero for the partial decay width $\Gamma_{\text{unknown}}$.

The rate of processes where a $Z^0$ boson mediates the interaction $e^+e^- \to f\bar{f}$ rather than a photon (i. e. the two Feynman diagrams on the left in fig. 1) is highest at center-of-mass energies near the mass of the $Z^0$ boson. This is evident from the fact that fermionic cross section $\sigma_f$ follow a relativistic Breit-Wigner distribution:

$$\sigma_f = \frac{12\pi\Gamma_e\Gamma_f}{s \cdot M_Z^2} \cdot |\chi(s)|^2 = \frac{12\pi}{M_Z} \cdot \frac{s\Gamma_e\Gamma_f}{\left(s - M_Z^2\right)^2 + \left(s^2\Gamma_Z^2/M_Z^2\right)}, \tag{2}$$

with the partial decay widths given by

$$\Gamma_f = \frac{N_c^f}{3}\alpha\left(M_Z^2\right) \cdot M_Z \cdot \left(v_f^2 + a_f^2\right) = \frac{N_c^f\sqrt{2}}{12\pi}G_fM_Z^3\left((g_V^f)^2 + (g_A^f)^2\right) \tag{3}$$
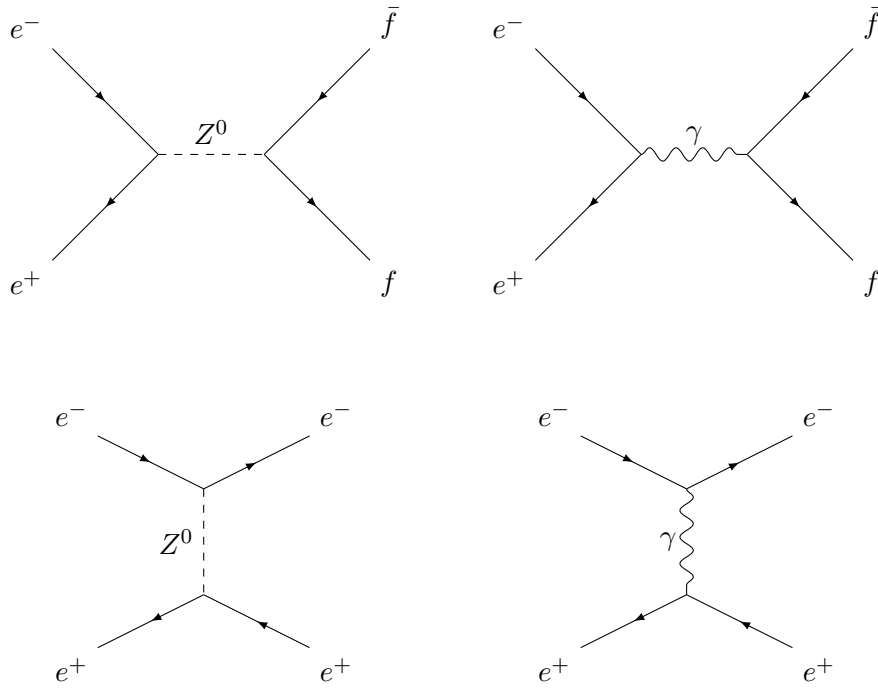
Figure 1: Shown are the lowest order Feynman diagrams for $e^+e^- \to f\bar{f}$ the top row shows the s-channel and bottom row the t-channel which is only possible if the finale state is $e^+e^-$.

There, the propagator $\chi$ is given by

$$\chi(s) = \frac{s}{(s - M_Z^2) + is\Gamma_Z/M_Z} \tag{4}$$

$N_c^f$ stands for the color factor and $Q_f$ for the electric charge of a fermion $f$. The symbol $s$ refers to the Mandelstam variable and can be written as square of the center-of-mass energy $E_{\text{com}}$, i.e. $s = E_{\text{com}}^2$. $v_f$ and $a_f$ are the vectorial and axial components of the matrix element of the process and depend on the fermion's quantum numbers $Q_f$ and $(I_3)_f$; the latter being the axial component of the fermion's isospin:

$$v_f = \frac{(I_3)_f - 2Q_f \sin^2\theta_W}{2\sin\theta_W\cos\theta_W} = \frac{g_V^f}{2\sin\theta_W\cos\theta_W}, \tag{5}$$

$$a_f = \frac{(I_3)_f}{2\sin\theta_W\cos\theta_W} = \frac{g_A^f}{2\sin\theta_W\cos\theta_W}. \tag{6}$$

$\theta_W$ is the Weinberg angle which describes the mixing angle between the original basis fields $B_0, W_0$ and the physical fields $\gamma$ and $Z_0$. Experimentally, $\cos\theta_W = M_W/M_Z$ describes the ratio between the mass of the $W^\pm$ boson and the mass of the $Z^0$ boson.

Note that in the case $f = e$ there is an additional contribution at lowest order: If the outgoing particles are given by an electron-positron pair, the incoming electrons can not just annihilate (this is the case of the diagram in the upper right in fig. 1) but also scatter (this is the diagram in th lower right in fig. 1). This implies that for the process $e^+e^- \to e^+e^-$ the contribution to the cross section is not only given by the $s$-channel, but also by the $t$-channel of the process. Which of these channel dominates depends on the scattering angle $\theta$, i.e. the angle between incoming and outgoing positively charged particle: For large scattering angles $\theta$ the $s$-channel is dominant while the $t$-channel dominates for small $\theta$. The dependence of the differential cross section of different channels with regard to the scattering angle can be written as $\frac{d\sigma}{d/}\cos\theta \propto 1 + \cos^2\theta$ in the $s$-channel case and $\frac{d\sigma}{d/}\cos\theta \propto (1 - \cos\theta)^{-2}$ in the $t$-channel case.

The quantum numbers and partial decay widths of every outgoing particle we consider are given in table 3. Summing each partial decay width multiplied by the number of particles in that row gives the total decay width of the $Z^0$ boson

$$\Gamma_Z = 2422.303\,\text{GeV}. \tag{7}$$

In that calculation, the Weinberg angle was set to $\sin^2\theta_W = 0.231\,21$ [4]. Further, for each particle a ratio is given between the total decay width of the $Z^0$ boson under the assumption that another member of that particles family would exist and the total decay width predicted by the Standard Model given by eq. (7). In addition, the theoretical total cross section of every particle's family was calculated using eq. (2) at the resonance center-of-mass energy $\sqrt{s} = M_Z$. As we don't differentiate up-type quarks from down-type quarks in our actual analysis, the total cross section and sum of partial widths have been performed over all five relevant quarks.

Table 3: Overview over the quantum numbers, decay widths, and cross sections of different particles. Note that the sum in the last two columns sum over all charged leptons, all neutrinos, and all quarks, in each row, respectively.

| Particle | $N_c^f$ | $(I_3)_f$ | $Q_f$ | $\Gamma_f$ [MeV] | $1 + \Gamma_f/\Gamma_Z$ | $\sum_f \Gamma_f$ [MeV] | $\sum_f \sigma_f$ [nb] |
|---|---|---|---|---|---|---|---|
| $e, \mu, \tau$ | 1 | $-\frac{1}{2}$ | $-1$ | 83.40 | 1.034 | 250.23 | 6.28 |
| $\nu_e, \nu_\mu, \nu_\tau$ | 1 | $\frac{1}{2}$ | 0 | 165.88 | 1.068 | 497.64 | 12.49 |
| $u, c$ | 3 | $\frac{1}{2}$ | $\frac{2}{3}$ | 285.40 | 1.118 | 1674.43 | 42.02 |
| $d, s, b$ | 3 | $-\frac{1}{2}$ | $-\frac{1}{3}$ | 367.87 | 1.152 | | |

### 2.2.1. Luminosity

The $t$-channel process can be used for the calculation of the luminosity $L$ of the experiment. By definition of the cross section $\sigma$ of any scattering process

$$\frac{\mathrm{d}n}{\mathrm{d}t} = \sigma L, \qquad n = \sigma \int L \, \mathrm{d}t, \tag{8}$$

holds where $L$ refers to the particle accelerator's luminosity and $\frac{\mathrm{d}n}{\mathrm{d}t}$ is the event rate of the process in question. That means that the luminosity of the experiment is needed to calculate the cross sections of the different processes from the number of events of the respective process. Since the cross section of the $t$-channel of the $e^+e^-$ process is well approximated by the theory, it can be used to calculate the luminosity. In the actual experiment, however, the integrated luminosity is provided for specific center-of-mass energies.

### 2.2.2. Forward-backward asymmetry

In this report the forward-backward asymmetry $A_{\mathrm{FB}}$ will be determined for muons. This quantity is especially useful as it provides an unostentatious way to compute the squared sine of the Weinberg angle, $\sin^2 \theta_\mathrm{W}$. The forward-backward asymmetry itself is a measure of the asymmetry of the process with respect to the beam direction and is defined via the differential cross section as

$$A_{\mathrm{FB}} = \frac{\int_0^1 \frac{\mathrm{d}\sigma_f}{\mathrm{d}\cos\theta} \, \mathrm{d}\cos\theta - \int_{-1}^0 \frac{\mathrm{d}\sigma_f}{\mathrm{d}\cos\theta} \, \mathrm{d}\cos\theta}{\int_0^1 \frac{\mathrm{d}\sigma_f}{\mathrm{d}\cos\theta} \, \mathrm{d}\cos\theta + \int_{-1}^0 \frac{\mathrm{d}\sigma_f}{\mathrm{d}\cos\theta} \, \mathrm{d}\cos\theta}. \tag{9}$$

At lowest order perturbation theory the differential cross section is given by

$$\frac{\mathrm{d}\sigma_f}{\mathrm{d}\cos\theta} = \frac{\alpha^2 N_c^f}{4s} \left( F_1(s) \left( 1 + \cos^2\theta \right) + 2F_2(s) \cos\theta \right), \tag{10}$$

with

$$F_1(s) = Q_f^2 - 2v_e v_f Q_f \Re(\chi(s)) + \left( v_e^2 + a_e^2 \right) \left( v_f^2 + a_f^2 \right) |\chi(s)|^2 \tag{11}$$

$$F_2(s) = -2a_e a_f Q_f \Re(\chi(s)) + 4v_e a_e v_f a_f |\chi(s)|^2. \tag{12}$$

Carrying out the integrations, the forward-backward asymmetry can be written as

$$A_{\text{FB}} = \frac{3}{4} \frac{F_2}{F_1}. \tag{13}$$

Exactly at the maximum, i. e. at $\sqrt{s} = M_Z$, the asymmetry can be expressed as

$$(A_{\text{FB}})_f(M_Z^2) = 3 \, \frac{(v/a)_e}{1 + (v/a)_e^2} \, \frac{(v/a)_f}{1 + (v/a)_f^2}. \tag{14}$$

Since the ratio $v_l/a_l = 1 - 4\sin^2\theta_W$ is very small the forward-backward asymmetry at the peak (for leptons) can be further approximated by

$$(A_{\text{FB}})_f(M_Z^2) \approx 3 \left(\frac{v_l}{a_l}\right)^2. \tag{15}$$

Thus, by measuring the forward-backward asymmetry at the resonance energy, a good estimation for the squared sine of the Weinberg angle can be obtained

## 2.3. The OPAL detector

The OPAL detector is made up of a number of components; a sectional view of the detector is shown in fig. 2. In the following, some of the main components and their function will be explained. The inner most part of the detector is the central detector whose components mainly are used to measure the tracks of charged particles and there momenta. In the central detector the component nearest to the collision point is the $\mu$-vertex-detector, followed by the vertex chamber again followed by the jet chamber and at the end the Z chamber. The inner detector is positioned within a cylindric pressure vessel which is surrounded by a solenoid which induces a harmonic magnetic field into the inner detector. After the solenoid follows a time of flight detector (TOF), which is a scintillator counter used to trigger events and measure the time of flight of the particles which can be used to calculate the particle's velocity. This all is surrounded by the electromagnetic calorimeter (ECAL) which consists of one barrel surrounding the central part and two end caps enclosing the outer parts at the beam pipe.

With this setup, 98 % of the solid angle is covered. The ECAL can measure the position and energy deposition of electromagnetic showers (which are triggered by photon through electromagnetic showering, electron and positron). Forward detectors are built into the end caps of the ECAL, which are used to measure luminosity by coincident detection of electrons and positrons at small angles. A hadron calorimeter (HCAL) is built around the ECAL which also consists of of a central barrel and two end caps. In this the energy deposition and position of a hadron shower can be measured. The outermost part is build from muon detectors which detect the position and direction of muons. For a more detailed description of the different parts of the OPAL and how they are build up one can have a look at ref. [2].
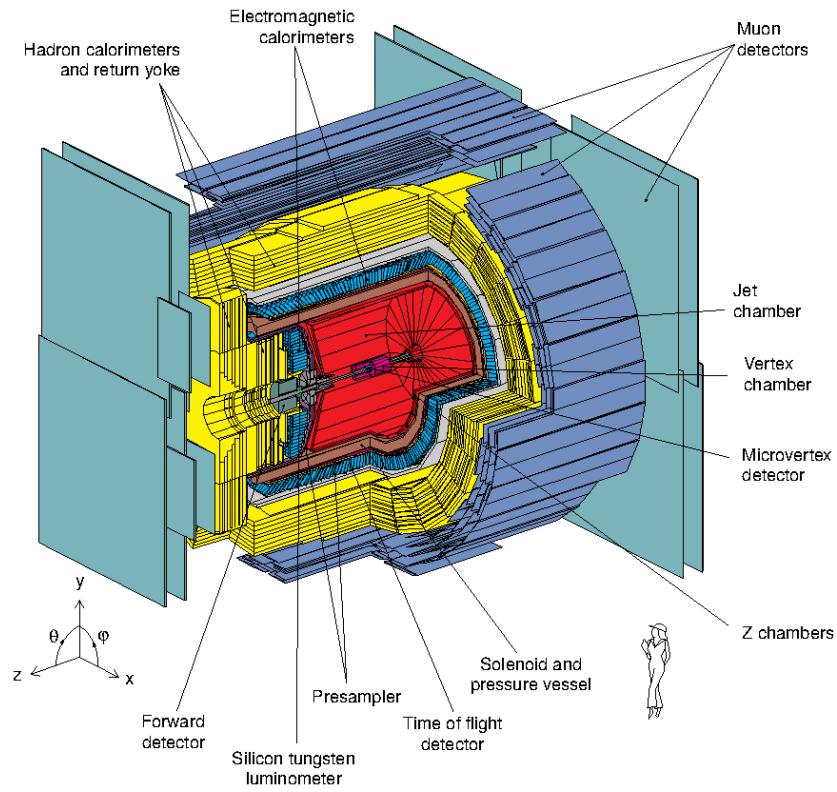
Figure 2: A sketch of the OPAL detector showing its components layer by layer [2].

## 2.4. Particle selection

The different particles produced by the collision of the beams can be detected and distinguished by the tracks they leave in the detectors. In the following paragraphs we focus on the different decay modes of the $Z^0$ boson and how the outgoing particles can be seen in the detector. A graphical overview of different particle tracks is given in fig. 3.

If the $Z^0$ boson decays in to a $e^+e^-$ pair the resulting particles both leave a track in the inner detector, so that two charged particles can be detected. Further, the sum of the momenta measured in the inner detector should be near to the beam energy as this is a relatively "clean" process. This is also the reason why the energy measured in the ECAL should be similar to the measured momenta and thus near the beam energy. Since the particles should have by now lost all their energy in the ECAL, the energy measured in the outer detectors should be close to zero.

If the $Z^0$ decays in a muon-antimuon pair, the signature measured in the inner detector is the same as for the electron-positron pair; however there should be near to no energy deposit into the ECAL or HCAL due to the high mass of muons.

Fully describing the tracks of an tau-antitau pair is a little bit more difficult since they decay extremely fast and can decay in a couple of different possible other particles. Therefore the number of charged particles and how much energy is deposit in which detector can differ. However, since the most prominent decays of the tau has neutrinos (which can carry a relatively large amount of energy) as end products the energy deposited in ECAL and HCAL should be quiet a bit lower than the beam energy. This is thus one possibility to separate them from muons or electrons.

In the case of a decay into quarks, it is quite hard to look out for special quarks, since they are not stable as single particles and therefore interact frequently with the detector hardware; however, this provides the possibility to separate hadronic events in general from lepton events. In the case of hadrons a large number of charged particles are detected, whereas for the leptonic events, only a few are produced. In general, a further separation of different hadrons is very well possible, but exceed the scope of the analysis done in this report.

If the $Z^0$ decays into neutrinos, we can not detect them since they do not interact with any of the detectors.

### 2.4.1. A note on Monte-Carlo based event selection

Before we start to try analyzing real detector data, we first look at simulated events. These events are created using Monte-Carlo based simulations of the behaviour of particles created inside the detector. This allows us to study specific signals the detector displays while knowing exactly which particles caused them. After a thorough investigation we arrive at a selection algorithm which takes detector events as input and assigns them some educated guess about which particle comes out after the collision. This selection algorithm, however, is not perfect in general. If $n_{ij}^{\mathrm{MC}}$ is the number of Monte-Carlo generated events of particles $j$ which are classified as en event of particle $i$ and $N_j^{\mathrm{MC}}$ is the total number of Monte-Carlo generated events of particle $j$, we can compute a
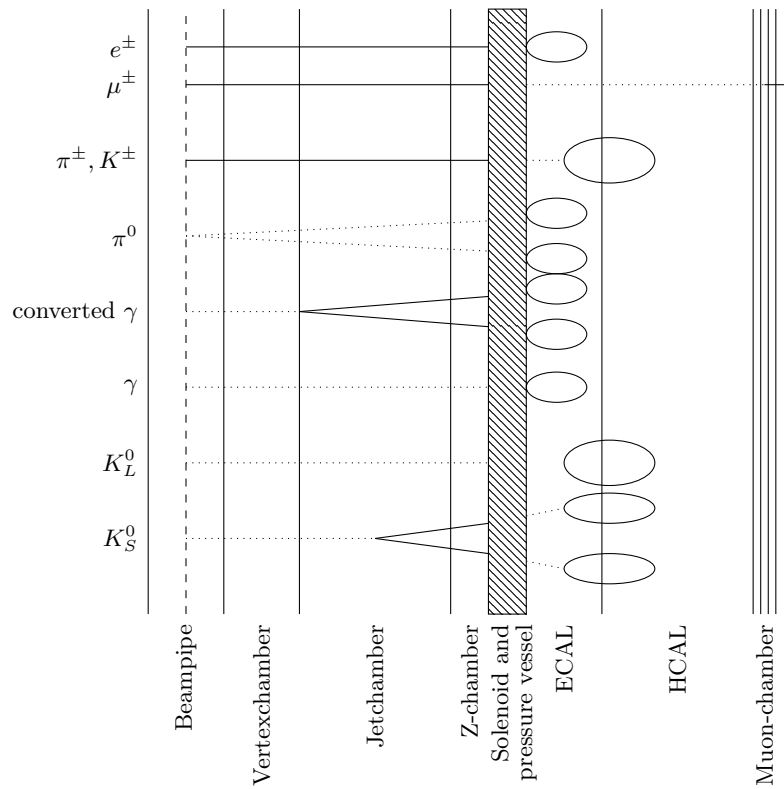
Figure 3: Examples of signals given by different particles in the opal detector. Adapted from the reference [8].

so-called efficiency

$$\epsilon_{ij} = \frac{n_{ij}^{\text{MC}}}{N_j^{\text{MC}}} \tag{16}$$

which is a measure of the goodness of our classification scheme.

Assuming our algorithm is perfect, the efficiencies $\epsilon_{ij}$ would be given by Kronecker symbols $\delta_{ij}$ as a particle of type $i$ would be classified as a particle of type $j$ if and only if $i = j$. This assumption, however, is not correct in general and the number of events our scheme classifies as being of type $i$ is given by

$$N_i = \sum_{j=1}^{n} \epsilon_{ij} N_j^{\text{MC}}, \tag{17}$$

or, as a matrix equation,

$$\begin{pmatrix} N_1 \\ \vdots \\ N_n \end{pmatrix} = \begin{pmatrix} \epsilon_{11} & \cdots & \epsilon_{1n} \\ \vdots & & \vdots \\ \epsilon_{n1} & \cdots & \epsilon_{nn} \end{pmatrix} \cdot \begin{pmatrix} N_1^{\text{MC}} \\ \vdots \\ N_n^{\text{MC}}, \end{pmatrix} = E \begin{pmatrix} N_1^{\text{MC}} \\ \vdots \\ N_n^{\text{MC}}, \end{pmatrix}, \tag{18}$$

where $E$ is the efficiency matrix.

In the case where we have to deal with the real OPAL data, the correct amounts of each particles created is unknown. We name these unknowns $\tilde{N}_i$ for each particle of type $i$. Instead, our classification scheme gives us guessed amounts $N_1, \ldots, N_n$. Yet, under the assumption that our Monte-Carlo data is accurate, the relationship between the actual numbers of created particles $\tilde{N}_1, \ldots, \tilde{N}_n$ and the numbers of particles classified by our algorithm is given by

$$\begin{pmatrix} N_1 \\ \vdots \\ N_n \end{pmatrix} = E \begin{pmatrix} \tilde{N}_1 \\ \vdots \\ \tilde{N}_n. \end{pmatrix} \tag{19}$$

That is, by inverting the above matrix-vector equation we can obtain the correct numbers of particles actually created in the detector:

$$\begin{pmatrix} \tilde{N}_1 \\ \vdots \\ \tilde{N}_n. \end{pmatrix} = E^{-1} \begin{pmatrix} N_1 \\ \vdots \\ N_n \end{pmatrix}. \tag{20}$$

Thus, one of our goals is to determine the efficiency matrix $E$ (or rather, its inverse $E^{-1}$) as accurately as possible. Once the inverse is calculated, the total cross sections can be obtained by dividing by the integrated luminosity $\mathfrak{L} = \int L \, \mathrm{d}t$:

$$\begin{pmatrix} \sigma_1 \\ \vdots \\ \sigma_n \end{pmatrix} = \frac{1}{\mathfrak{L}} \begin{pmatrix} \tilde{N}_1 \\ \vdots \\ \tilde{N}_n \end{pmatrix} = \frac{1}{\mathfrak{L}} E^{-1} \begin{pmatrix} N_1 \\ \vdots \\ N_n \end{pmatrix}. \tag{21}$$

# 3. Methodology and Analysis

## 3.1. First event analysis using GROPE

For a first rough analysis the application GROPE [10] was used. Grope visualizes a tidy selection of detector events by drawing detected tracks and displaying a summary of the event data which allows to find event selection criteria to distinguish different particles. Not only can different pre-selected event collections be selected, but the tracks can be visualized in three dimensions.

Figure 4 gives an overview of the optical reconstruction of some events in the OPAL detector: The behaviour of the different particles explained in section 2.4 can be nicely recognized in the pictures. For example, it can be seen that the electron and muon event both show two opposing charged tracks in the inner detector, but at the electron event the energy mostly is deposit into the ECAL (shown as blue cuboids) and for the muon event nearly no energy is deposit into the ECAL or HCAL but, following the path of the charged particles in the inner detector, the associated signals in the muon detectors can be observed.

One can also evaluate some of the measurement variables statistically by creating histograms to figure out which can be used to determine which events can be assigned to which particles. The variables on which the histograms are based are briefly explained in the following: E.ECAL and E.HCAL refer to the total amount of energy deposited in the electromagnetic and hadronic calorimeter, respectively. The total scalar sum of the momenta of charged particles determined by the inner detector (i.e. the sum of all absolutes of the momentum vectors) is called P.CHARGED. N.CHARGED is the total number of charged particles detected by the inner detector. Similarly, N.MUON is the number of muons detected by the muon detectors.

Exemplary histograms are shown in fig. 5. It can be seen that hadronic and leptonic events could be separated quite well using the number of charged particles since only hadron events seem two have more than about 15 charged tracks. For the distinction between muonic events and electron and tau events one could use the ratio between P.CHARGED and E.ECAL (which we call RATIO in the following) since it seems to be near to one for the electrons and tau and to be mostly higher as five for the muon. In addition, an additional cut using the number of muon signals (N.MUON) could be helpful, but this data will not be provided later in the Monte-Carlo and OPAL data so it can not be used for an effective separation. For the separation between tau and electrons the energy deposition in the ECAL seems to be a quite good variable for a cut. The energy deposition into the HCAL, on the other hand, seems to be to mixed up to use it for a satisfying cut.

## 3.2. Setting cuts using the Monte-Carlo data

The Monte-Carlo data is structured similarly to the data we gathered in the statistical data analysis using GROPE data. The variable names defined in the previous section will thus be used throughout this analysis. Additionally, there is also COS.THRU which, in the case of hadronic events, refers to the cosine of the thrust axis, and COS.THET

Figure 4: The reconstruction of the detector events done by grope are shown. In the upper left one sees an electron-positron event, in the upper right a muon-anti-muon event is shown, in the bottom left a tau-anti-tau event is shown and in the bottom right a hadron event is shown.
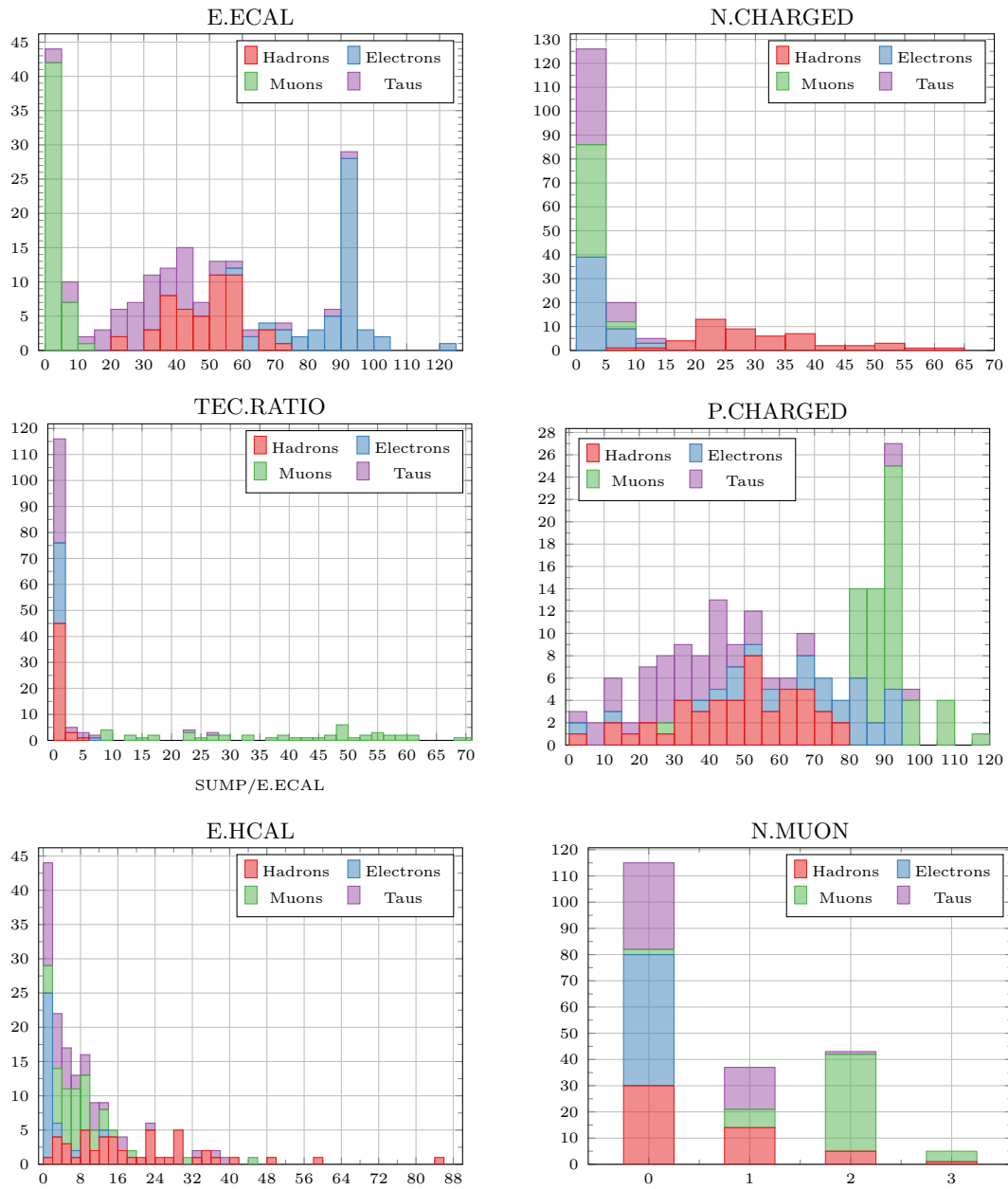
Figure 5: The histograms of the grope data for the four different event types.

which, in the case of leptonic events, refers to the cosine of the angle of the outgoing positively charged particle to the incoming positron beam.

### 3.2.1. Separating the different particle events

Using the Monte-Carlo data we first created histograms similar to what we have done for the GROPE data and tried to find some satisfying cuts. In fig. 6 histograms visualizing different measurement values are shown.

As seen before for the GROPE data the hadronic events and leptonic events can be nicely separated by the number of charged tracks. The cut was set that every event showing seven or more charged track was identified as a hadron event and every event with strictly less than seven charged tracks was guessed to be a lepton event.

To separate the lepton events the ratio between P.CHARGED and the energy deposition in the ECAL was considered (see the last plot in fig. 6). Unlike the GROPE data, however, the ratio does not seem to be suitable for a cut in the Monte-Carlo data. The bump in the muon data at a ratio of zero is given by the bump for the sum of the momenta at zero. This bump could be reasoned by the fact that if the muonic scattering angle is too small the inner detector can not correctly detect their momenta (e.g. due to a lack of coverage of that detector volume). However, by closely inspecting the particles with vanishing P.CHARGED, one finds that all other observables seem to be distributed just like those of the particles with non-vanishing P.CHARGED, with the exception of the cosine of the scattering angle COS.THET which seems to be close to either $-1$ or $1$. Further, for muonic events one obtains an N.CHARGED around 2 (as expected), implying that the inner detector seems to be working. Different observations of the Monte-Carlo data set with events where P.CHARGED vanishes can be seen in the appendix in figs. 13 and 14.

Another possibility to separate the leptons is to look at the energy deposition into the ECAL: It can clearly be seen that electrons deposit the most energy into the ECAL so it was decided to separate the electrons from the other leptons by cutting the leptons at ECAL $= 70\,\mathrm{GeV}$. Each event with an energy deposition higher or equal to $70\,\mathrm{GeV}$ is treated as a electron event. Now that electrons and hadrons are dealt with, muon and tau events need to be separated. This was done by once doing a cut in the ECAL energy and at the same time doing a cut in the sum of the momenta. If an event has an energy deposition into the ECAL smaller as $25\,\mathrm{GeV}$ and at the same time the sum of the momenta is either greater or equal $70\,\mathrm{GeV}$ or equal to $0\,\mathrm{GeV}$ it was selected as a muon event otherwise it was selected as a tau event. The reasoning for this cuts can be nicely seen in a two dimensional histogram as shown in fig. 7.

The last important variable of measurement to look at is $\cos\theta$, with $\theta$ for leptons being the angle between the positive lepton to the positron beam direction and for the hadron events the angle of the thrust axis. This variable is shown in fig. 8. For the hadronic, muonic and tau final states the distribution shows the expected $1 + \cos\theta^2$ $s$-channel behaviour nicely. The electronic final state events show an overlapping of the $s$-channel and the $t$-channel ($(1 - \cos\theta)^{-2}$) behaviour as expected. It should be noted that for some of the events the detection mechanism was not able to compute a value
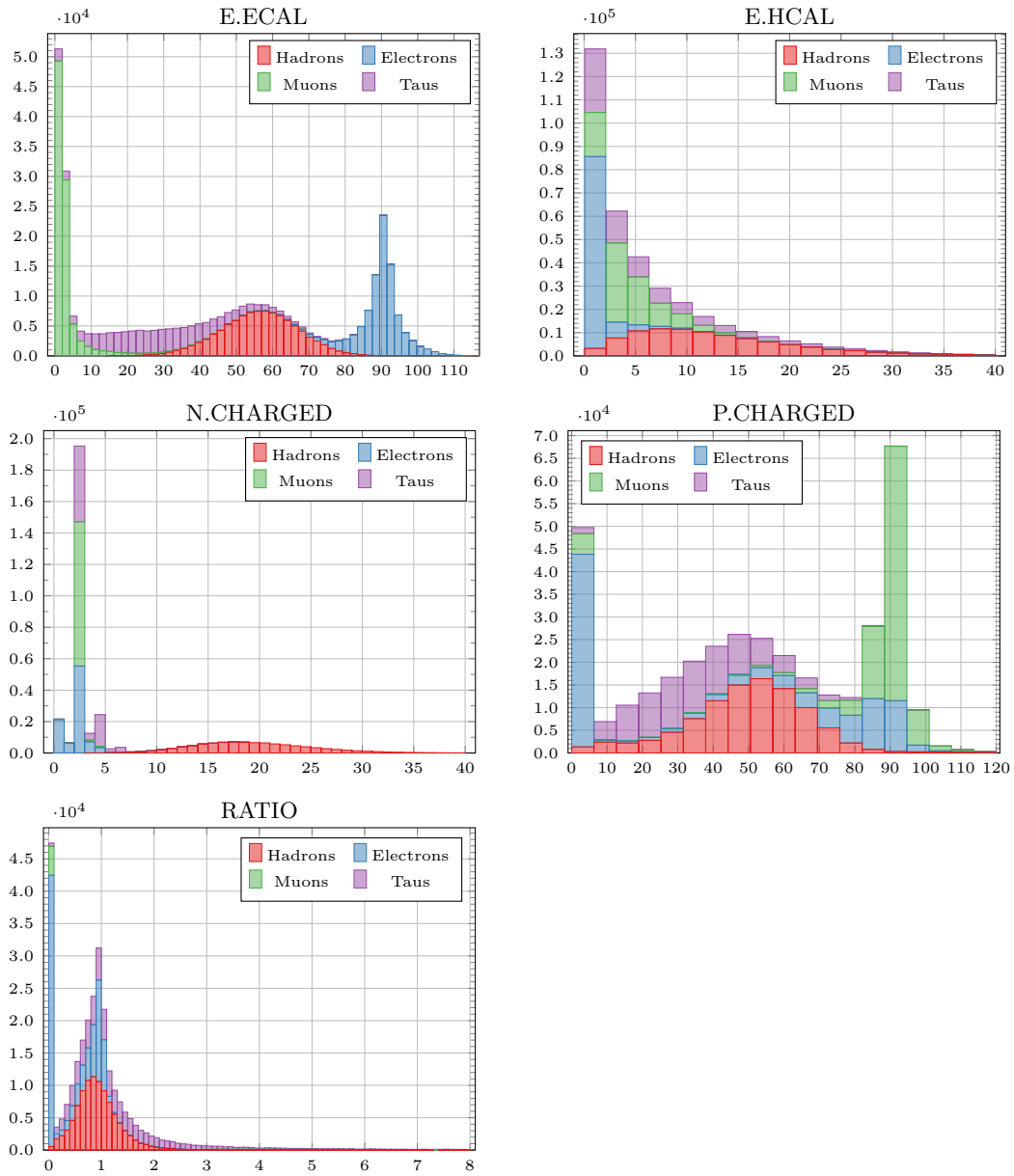
Figure 6: Histogram for different measurement variables for the different particles using the Monte-Carlo data. It should be noted that the plot of RATIO (lower left) cuts away most of the muon data which mostly has a ratio > 8. This is done so that the peak of muon events at a ratio of zero can be identified.

for COS.THET; these events are not shown in the angular distributions. These events however do show normal behaviour in the other variables, so that they can be used as long as no information about $\theta$ is needed.
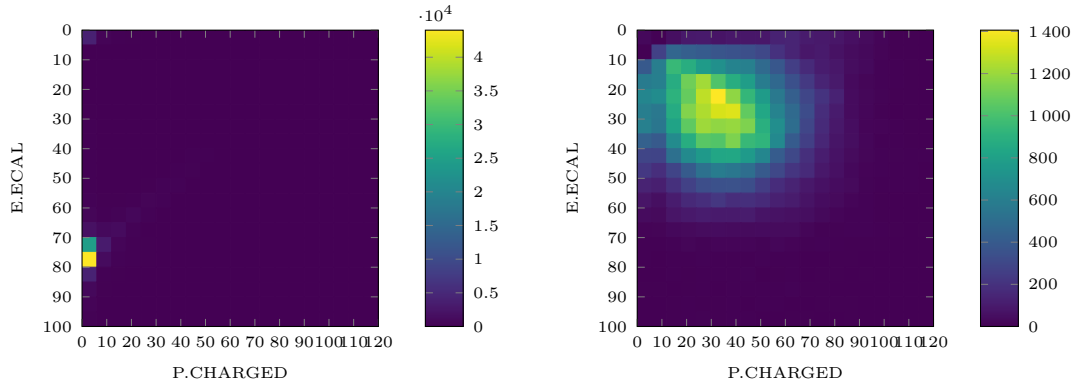


Figure 7: Separation of muonic and tau events by considering the two-dimensional distribution of P.CHARGED and E.ECAL.

### 3.2.2. Calculating the efficiency matrix

In order to evaluate the quality of our cuts and to be able to estimate the actual number of events from the OPAL data later on, the efficiency matrix

$$
E = \begin{pmatrix}
\epsilon_{ee} & \epsilon_{e\mu} & \epsilon_{e\tau} & \epsilon_{eh} \\
\epsilon_{\mu e} & \epsilon_{\mu\mu} & \epsilon_{\mu\tau} & \epsilon_{\mu h} \\
\epsilon_{\tau e} & \epsilon_{\tau\mu} & \epsilon_{\tau\tau} & \epsilon_{\tau h} \\
\epsilon_{he} & \epsilon_{h\mu} & \epsilon_{h\tau} & \epsilon_{hh}
\end{pmatrix}
\tag{22}
$$

was calculated. The indices $e, \mu, \tau, h$ represent electron, muon, tau and hadron events, respectively. Recall that the efficiencies $\epsilon_{ij}$ are defined by

$$
\epsilon_{ij} = \frac{n_{ij}^{\mathrm{MC}}}{N_j^{\mathrm{MC}}}
\tag{23}
$$

where $n_{ij}^{\mathrm{MC}}$ is the number of events of particle $j$ which are classified by our cuts as an event of particle $i$ and $N_j^{\mathrm{MC}}$ is the total number of events of particle $j$. Important to note is, that not the length of the dataset given for each particle was used as $N_j^{\mathrm{MC}}$ but instead the fixed value $100\,000$, which also takes into account internal processes of the simulations. The cuts that we initially chose were optimized by small variations of the numeric cut limits. Our goal at this stage was to approximate an identity matrix with our efficiency matrix, as that would be an efficiency matrix for a perfect particle selection algorithm. Thus, we required our diagonal matrix elements to be as close to one as possible and non-diagonal matrix elements to preferably vanish. With this we
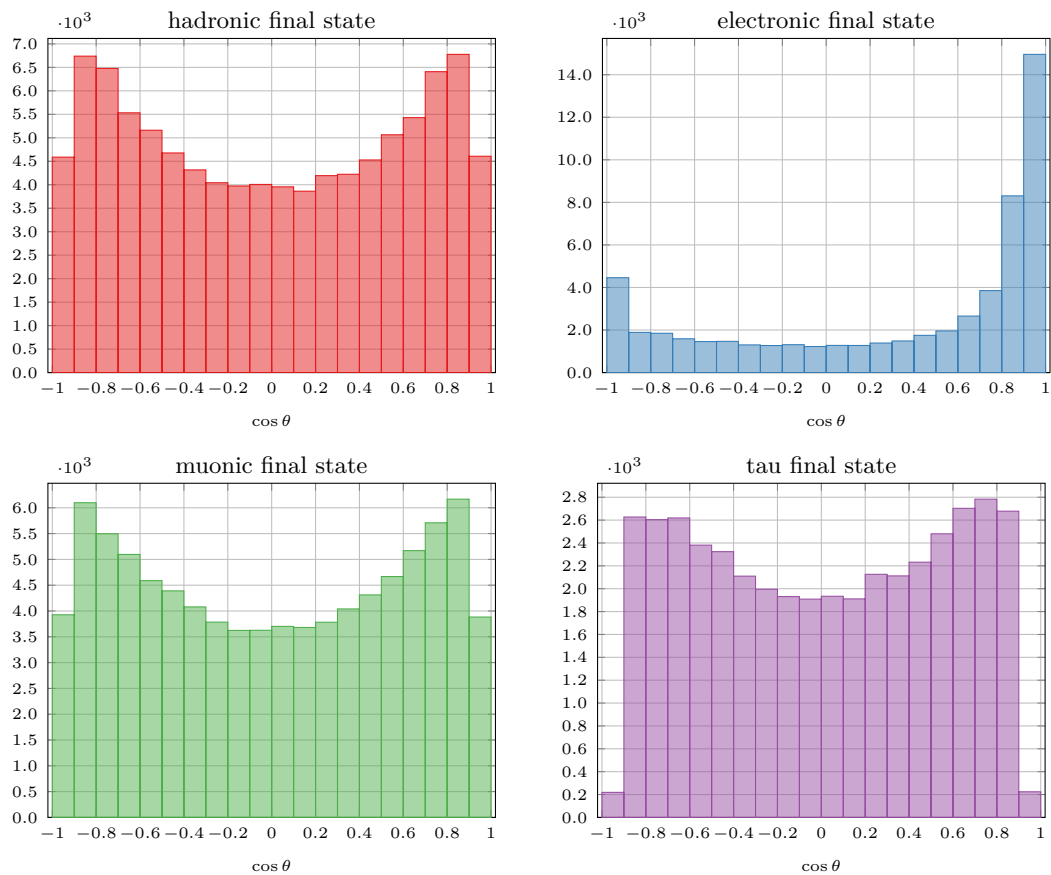
Figure 8: For the three different leptons the histogram of the cosine of the angle between the positive lepton and the positron beam direction and for the hadronic final states the angle of the thrust axis.

got the cuts with the cut limits as mentioned above, which are just small deviations of the cuts we chose initially. Numerically, our efficiency matrix reads as follows:

$$E = \begin{pmatrix} 9.2097 \cdot 10^{-1} & 0 & 3.18 \cdot 10^{-3} & 2.5 \cdot 10^{-4} \\ 1.0 \cdot 10^{-5} & 9.1224 \cdot 10^{-1} & 2.859 \cdot 10^{-2} & 0 \\ 8.4 \cdot 10^{-3} & 8.09 \cdot 10^{-3} & 7.4954 \cdot 10^{-1} & 9.76 \cdot 10^{-3} \\ 3.4 \cdot 10^{-4} & 0 & 4.76 \cdot 10^{-3} & 9.8043 \cdot 10^{-1} \end{pmatrix} \tag{24}$$

In addition to the efficiencies itself, errors for the efficiencies were calculated, too. To do so, we assumed $n_{ij}^{\mathrm{MC}}$ and $N_j^{\mathrm{MC}}$ to be distributed following a Poisson distribution: As our selection is basically a counting experiment with large sample size and low probability to miscount, this assumption seems reasonable. The Maximum-Likelihood estimator for the standard deviation of Poisson-distributed variable is given by its square root, i. e. we set the uncertainty on $n_{ij}^{\mathrm{MC}}$ and $N_j^{\mathrm{MC}}$ to be $\sqrt{n_{ij}^{\mathrm{MC}}}$ and $\sqrt{N_j^{\mathrm{MC}}}$, respectively. By propagating this uncertainty we obtain the following formula for the uncertainty of the efficiencies:

$$\sigma_{\epsilon_{ij}} = \sqrt{\frac{n_{ij}^{\mathrm{MC}}}{\left(N_j^{\mathrm{MC}}\right)^2} + \frac{\left(n_{ij}^{\mathrm{MC}}\right)^2}{\left(N_j^{\mathrm{MC}}\right)^3}} \tag{25}$$

which results in the following error matrix for the efficiencies:

$$\sigma_E = \begin{pmatrix} 4 \cdot 10^{-3} & 0 & 1.8 \cdot 10^{-3} & 5 \cdot 10^{-5} \\ 1.0 \cdot 10^{-5} & 4 \cdot 10^{-3} & 5 \cdot 10^{-4} & 0 \\ 3 \cdot 10^{-4} & 3 \cdot 10^{-4} & 4 \cdot 10^{-4} & 3 \cdot 10^{-3} \\ 6 \cdot 10^{-5} & 0 & 2 \cdot 10^{-3} & 4 \cdot 10^{-4}. \end{pmatrix} \tag{26}$$

### 3.2.3. *s*-channel separation

In having separated the different particles we now also need to separate the *s*-channel and *t*-channel for the electronic decay channel. This can be done using the distribution of the scattering angle or the cosine of the angle, which is how it is given in the data. A histogram of the cosine distribution is shown in fig. 9. As electron scattering corresponds to shallow angles (these are angles whose cosine is close to $\pm 1$), the *s*-channel can be selected by only choosing events where COS.THET $\in [u, l]$ where $u$ and $l$ are the upper and lower bounds that we have to choose for best selection efficiency. To separate the channels we start by fitting the function

$$F(x) = A\left(1 + x^2\right) + \frac{B}{(1 - x)^2} \tag{27}$$

at the histogram using the least squares fitting method `curvefit` from the python module `scipy.optimize` [3] which was supplied with the Poisson errors on the cosine bins.
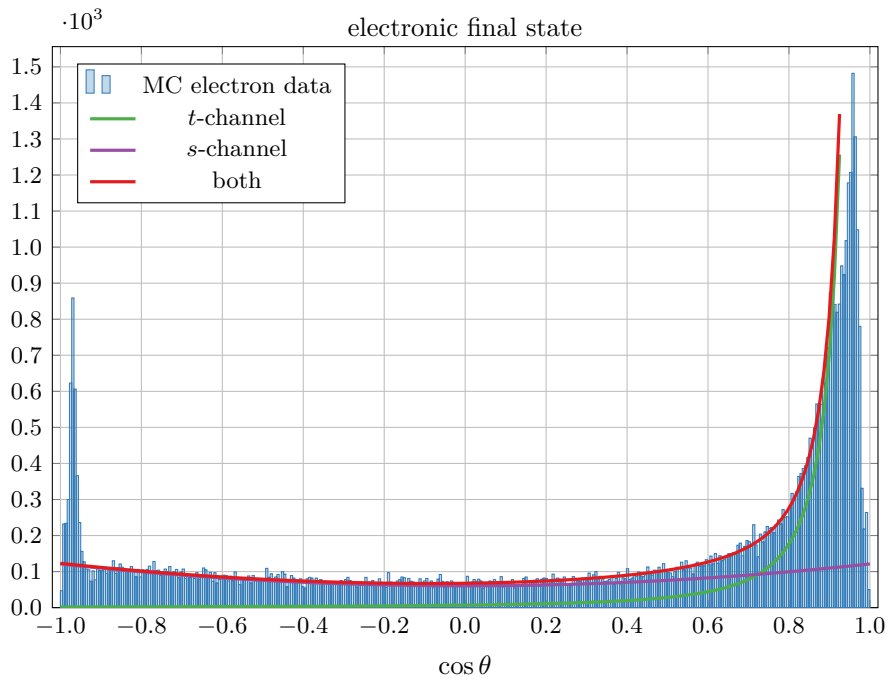
Figure 9: The histogram for $\cos\theta$ for the electronic events. Also shown a fit of the form eq. (27) and the single $s$-channel and $t$-channel distributions using the results of the fit.

*3. Methodology and Analysis*

This fit is also plotted into fig. 9, we get the results

$$A = 60.6 \pm 0.5, \tag{28}$$

$$B = 7.06 \pm 0.10, \tag{29}$$

$$\begin{pmatrix} \text{cov}(A,A) & \text{cov}(A,B) \\ \text{cov}(B,A) & \text{cov}(B,B) \end{pmatrix} = \begin{pmatrix} 0.294 & -0.024 \\ -0.024 & 0.011 \end{pmatrix}. \tag{30}$$

Using this we can calculate an efficiency for the $s$-channel selection by calculating

$$\epsilon_s = \frac{\int_l^u \frac{\mathrm{d}\sigma_s}{\mathrm{d}\cos\theta}(x)\,\mathrm{d}x}{\int_l^u F(x)\,\mathrm{d}x} \tag{31}$$

where $\frac{\mathrm{d}\sigma_s}{\mathrm{d}\cos\theta}(x) = A\left(1+x^2\right)$ is the distribution of the $s$-channel and $l$ and $u$ are the boundaries of the section we want to cut out. By choosing upper and lower bounds such that the efficiency is the highest will result in a high cleanliness rate of electrons from the $s$-channel. However, by this picky selection of $s$-channel electrons, a lot of $s$-channel electrons will be discarded leading to a skewed counting rate. To evade this problem we multiply the number of guessed $s$-channel electrons by the following correction factor:

$$r = \frac{\int_{-1}^1 \frac{\mathrm{d}\sigma_s}{\mathrm{d}\cos\theta}(x)\,\mathrm{d}x}{\int_l^u \frac{\mathrm{d}\sigma_s}{\mathrm{d}\cos\theta}(x)\,\mathrm{d}x} = \frac{A\left[\frac{x^3}{3}+x\right]_{-1}^1}{A\left[\frac{x^3}{3}+x\right]_l^u} = \frac{\left[\frac{x^3}{3}+x\right]_{-1}^1}{\left[\frac{x^3}{3}+x\right]_l^u} = \frac{8}{u^3 - l^3 + 3(u-l)}. \tag{32}$$

$r$ gives the ratio between the total number of $s$-channel electrons and those that are actually selected by a cut. That means, if we multiply the number of $s$-channel electron events after the cut with this number, we should gain the actual number of $s$-channel electron events that happened. As boundaries we have chosen $l = 0.9$ and $u = 0$ which results in

$$\epsilon_s = 0.9539 \pm 0.0009, \qquad r = 2.3330. \tag{33}$$

For the ratio $r$ no error can be calculated since it just depends on the chosen boundaries which means that this ratio is exact. For the efficiency $\epsilon_s$, the error was calculated using the covariance matrix of the fit also given above.

Now, our original efficiency matrix given in eqs. (22) and (24) must be corrected by multiplying the efficiency $\epsilon_s$ of the $s$-channel to the first column of the matrix. The errors for the affected entries is propagated by

$$\sigma_{\epsilon_{ij}} = \hat{\epsilon}_{ij}\epsilon_s \cdot \left( \frac{\sigma_{\epsilon_s}}{\epsilon_s} + \frac{\sigma_{\hat{\epsilon}_{ij}}}{\hat{\epsilon}_{ij}} \right), \tag{34}$$

where $\hat{\epsilon}$ indicates the old efficiencies and $\epsilon_s$ the $s$-channel efficiency. This results in the

corrected efficiency matrix and error matrix

$$E = \begin{pmatrix} 8.786 \cdot 10^{-1} & 0.000 & 3.180 \cdot 10^{-3} & 2.500 \cdot 10^{-4} \\ 9.539 \cdot 10^{-6} & 9.122 \cdot 10^{-1} & 2.859 \cdot 10^{-2} & 0.000 \\ 8.013 \cdot 10^{-3} & 8.090 \cdot 10^{-3} & 7.495 \cdot 10^{-1} & 9.760 \cdot 10^{-3} \\ 3.243 \cdot 10^{-4} & 0.000 & 4.760 \cdot 10^{-3} & 9.804 \cdot 10^{-1} \end{pmatrix}, \quad (35)$$

$$\sigma_E = \begin{pmatrix} 4.842 \cdot 10^{-3} & 0.000 & 1.786 \cdot 10^{-4} & 5.001 \cdot 10^{-5} \\ 9.549 \cdot 10^{-6} & 4.177 \cdot 10^{-3} & 5.423 \cdot 10^{-4} & 0.000 \\ 2.852 \cdot 10^{-4} & 2.856 \cdot 10^{-4} & 3.621 \cdot 10^{-3} & 3.139 \cdot 10^{-4} \\ 5.594 \cdot 10^{-5} & 0.000 & 2.187 \cdot 10^{-4} & 4.406 \cdot 10^{-3} \end{pmatrix} \quad (36)$$

### 3.2.4. Inversion of the efficiency matrix and its error

To calculate the estimations of the actual number of events for each particle out of the OPAL data given we need to multiply the inverse of the efficiency matrix to the number of events for each particle we gain after applying our cuts to the OPAL data (see section 2.4.1 for more details). While the inverse $E^{-1}$ of the efficiency matrix can be calculated straightforward to be

$$\begin{pmatrix} 1.138 & 4.283 \cdot 10^{-5} & -4.829 \cdot 10^{-3} & -2.421 \cdot 10^{-4} \\ 3.694 \cdot 10^{-4} & 1.097 & -4.183 \cdot 10^{-2} & 4.163 \cdot 10^{-4} \\ -1.217 \cdot 10^{-2} & -1.184 \cdot 10^{-2} & 1.335 & -1.328 \cdot 10^{-2} \\ -3.175 \cdot 10^{-4} & 5.745 \cdot 10^{-5} & -6.479 \cdot 10^{-3} & 1.020 \end{pmatrix}$$
$$(37)$$

the calculation of the errors of the inverse matrix is more elaborate and will be presented in the following paragraphs.

We started with a numerical study by creating a large number $(500\,000)$ of $4 \times 4$-matrices containing random numbers. The random number at $i,j$ was distributed following a normal distribution with a mean given by the $i,j$th entry of the efficiency matrix $\epsilon_{ij}$ and variance $\sigma_{\epsilon_{ij}}^2$. At this point, one could argue, that the assumption of a normal distribution is inaccurate as each of the $\epsilon_{ij}$ can by its definition only take on discrete values due to the Monte-Carlo sample being finite. However, we justify this approximation by appealing to an argument involving the central limit theorem keeping the large number of toy experiments in mind.

Each of the resulting $500\,000$ random matrices were inverted and the distribution of each entry was examined; these distributions are visualized in fig. 10. One can see that the distribution of each element of the inverse matrix follows roughly a normal distribution. The red line in each plot corresponds to the probability density function of a normal distribution (scaled each histogram's frequencies). The mean and the standard deviation of each of these normal distributions was estimated using Maximum-Likelihood estimators, i. e. sample mean and (Bessel corrected) sample variance. The variances (or rather, their square roots) were used for the error on the efficiency matrix' inverse given
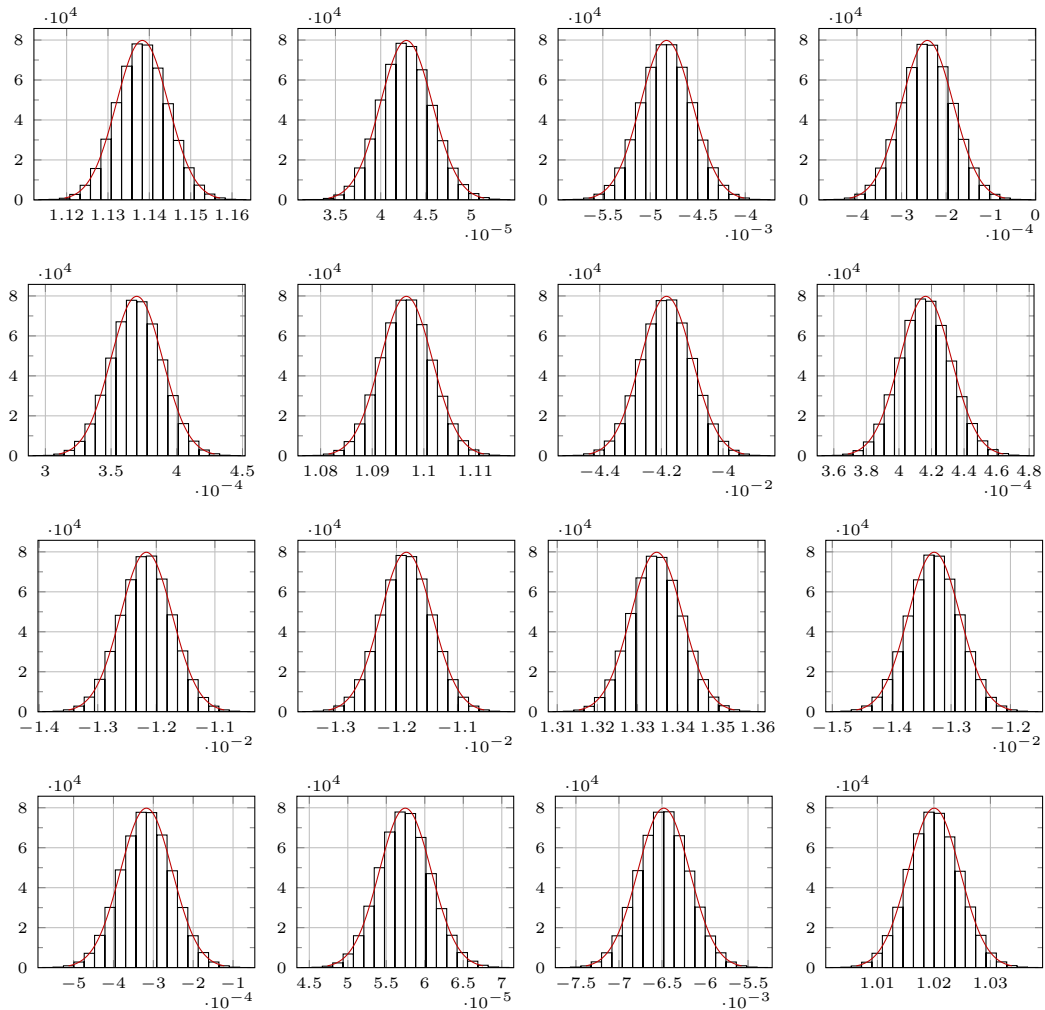
Figure 10: Monte Carlo study of the distribution of the elements of an inverted matrix originally consisting of normally distributed random numbers. Each histogram shows the distribution of its corresponding element of the inverse matrix. The red line shows the probability density of a Gaussian (scaled to frequencies) with parameters estimated using the Maximum-Likelihood estimators for mean and variance. Please note the axis scaling of each diagram.

24

in eq. (37). Thus, the error on $E^{-1}$ is given by

$$\sigma_{E^{-1}} = \begin{pmatrix} 6.274 \cdot 10^{-3} & 2.868 \cdot 10^{-6} & 2.739 \cdot 10^{-4} & 5.823 \cdot 10^{-5} \\ 1.974 \cdot 10^{-5} & 5.013 \cdot 10^{-3} & 8.409 \cdot 10^{-4} & 1.591 \cdot 10^{-5} \\ 4.421 \cdot 10^{-4} & 4.255 \cdot 10^{-4} & 6.455 \cdot 10^{-3} & 4.364 \cdot 10^{-4} \\ 6.506 \cdot 10^{-5} & 3.369 \cdot 10^{-6} & 3.013 \cdot 10^{-4} & 4.579 \cdot 10^{-3} \end{pmatrix}. \tag{38}$$

There is an alternative way to calculate the error on $E^{-1}$ which we will use to cross-check the result in eq. (38). If we assume the covariance of the elements of the efficiency matrix to vanish, the errors on the elements of $E^{-1}$ are given by [5]

$$\tilde{\sigma}_{E^{-1}} = \left( \sqrt{\sum_{i=1}^{4} \sum_{j=1}^{4} (E^{-1})_{\alpha i}^2 (\sigma_E)_{ij}^2 (E^{-1})_{j\beta}} \right)_{\substack{1 \le \alpha \le 4 \\ 1 \le \beta \le 4}}$$

$$= \begin{pmatrix} 6.274 \cdot 10^{-3} & 2.866 \cdot 10^{-6} & 2.737 \cdot 10^{-4} & 5.817 \cdot 10^{-5} \\ 1.973 \cdot 10^{-5} & 5.022 \cdot 10^{-3} & 8.412 \cdot 10^{-4} & 1.590 \cdot 10^{-5} \\ 4.424 \cdot 10^{-4} & 4.253 \cdot 10^{-4} & 6.451 \cdot 10^{-3} & 4.364 \cdot 10^{-4} \\ 6.508 \cdot 10^{-5} & 3.362 \cdot 10^{-6} & 3.008 \cdot 10^{-4} & 4.585 \cdot 10^{-3} \end{pmatrix}. \tag{39}$$

Thus, the exact result is in agreement with the result of our numeric study given in eq. (38). The small numeric deviations likely stem from the statistical nature of the execution of the Monte-Carlo based study.

Immediately from the fit results in table 4 we can obtain an estimate for the mass of the $Z^0$ boson by taking the weighted mean

$$M_Z = \frac{\sum_{f=e,\mu,\tau,h} (M_Z)_f \cdot \sigma_{(M_Z)_f}^{-2}}{\sum_{f=e,\mu,\tau,h} \sigma_{(M_Z)_f}^{-2}} = (91.19 \pm 0.05)\,\text{GeV/c}^2. \tag{40}$$

In the equation above, $(M_Z)_f$ refers to the value for $M_Z$ given in the row of particle $f$ in table 4. The error on our weighted mean for $M_Z$ was estimated by the standard deviation for the sample mean, that is, we divided the sample standard deviation by $\sqrt{n} = 2$ and used that as error for $M_Z$. We justify this conservative error estimation by the observation that the errors for the different fit results differ by one order of magnitude even though the fit method is the same and our goodness-of-fit estimates don't seem to correlate well with the errors.

## 3.3. The OPAL data

Now that the cuts are set and the efficiency matrix, its inverse as well as their errors are calculated, we proceed to analyze the real OPAL data. Plots similar to the ones already shown for the Monte-Carlo data are given in the appendix in figs. 15 and 16.

### 3.3.1. Breit-Wigner fits

First the given OPAL data was separated using the cuts defined with the Monte-Carlo data, i.e. each event of the OPAL data was assigned a guess variable containing the particle type assigned by our cuts. Events that are not selected by any cuts are discarded. Afterwards the data was grouped by the beam energies for which the luminosity was given. It should be noted that the actual beam energies for the OPAL data is not strictly the same as the once for which the luminosity was given but rather differ by a small amount from the energies in the luminosity data. For further calculation this difference was ignored and the beam energy was set to the nearest energy in the luminosity data frame. To be on the safe side we calculated the standard deviation for each group of beam energies assigned to one energy in the luminosity data. Using this sorted data the cross sections were calculated using

$$
\begin{pmatrix} \sigma_e \\ \sigma_\mu \\ \sigma_\tau \\ \sigma_h \end{pmatrix} = \frac{1}{\mathfrak{L}} E^{-1} \begin{pmatrix} N_e \\ N_\mu \\ N_\tau \\ N_h \end{pmatrix} + \text{corrections}
\tag{41}
$$

for each beam energy separately. "corrections" is a beam-energy dependent correction term responsible for the radiation corrections. It can be found the appendix in table 9.

Further, in the equation above, $\mathfrak{L}$ is the integrated luminosity and $e$, $\mu$, $\tau$ and $h$ describe electron, muon, tau and hadron events. The errors were calculated by error propagation

$$
\sigma_{\sigma_i} = \sqrt{\left(\frac{\sigma_i}{\mathfrak{L}}\sigma_\mathfrak{L}\right)^2 + \sum_{j=e,\mu,\tau,h} \left(\left(\sigma_i - \frac{\epsilon_{ij}N_j}{\mathfrak{L}}\right)\sigma_{N_j}\right)^2 + \sum_{j=e,\mu,\tau,h} \left(\left(\sigma_i - \frac{\epsilon_{ij}N_j}{\mathfrak{L}}\right)\sigma_{\epsilon_{ij}}\right)^2}.
\tag{42}
$$

For each particle the cross sections are plotted against the according beam energies (see fig. 11) and relativistic Breit-Wigner functions of the form

$$
\sigma_f(E_{\text{com}}) = \frac{12\pi}{M_Z^2} \frac{E_{\text{com}}^2 \Gamma_e \Gamma_f}{(E_{\text{com}}^2 - M_Z^2)^2 + E_{\text{com}}^4 \frac{\Gamma_Z^2}{M_Z^2}}
\tag{43}
$$

were fitted against this data using the non-linear least squares fit `nls` from `R` [7] which was supplied with the error on the cross sections. After a visual inspection of the ratio between errors on the cross section and the errors on the center-of-mass energies we decided that the latter was negligible for the non-linear least squares fit. This way we extracted $\Gamma_e \Gamma_f$, $M_Z$, and $\Gamma_Z$ for each of the four outgoing particle types as fit parameters. The values of the fit parameters are given in table 4 alongside their errors which were extracted from the covariance matrix supplied from the fit.

Further, a residual standard error (denoted here as $\chi^2/\text{df}$) was calculated for each fit and also given in table 4. As a rule of thumb, a residual standard error close to one is an indication of a good fit – if the value is much larger than one, the model doesn't fit the

data very well while a value much smaller than one is a sign of over-fitting. Although our degrees of freedom are only four, the residual standard errors obtained are quite good. To further understand the fit we also calculated test statistics alongside their $p$-values for each fit parameter of each fit. This was done by constructing the $t$-statistic of each parameter of each fit and finding the (two-sided) quantile of the $t$-distribution with four degrees of freedom. The results are given in table 5. The observation that all $p$-values are smaller than $10^{-4}$ indicates a great significance of each fit parameter. Interestingly, the fit parameter with the highest significance by far is $M_Z$ whose $p$-values lie below the $p$-values of other parameters by several orders of magnitude. This extreme difference in orders of magnitude suggests that an estimation of the mass of the $Z^0$-boson is easier (geometrically, the mass of the $Z^0$-boson falls together with the location of the peak of the Breit-Wigner distribution) and can be done with more accuracy than the other fit parameters. All in all, the low $p$-values suggest that our curve fits the data nicely.
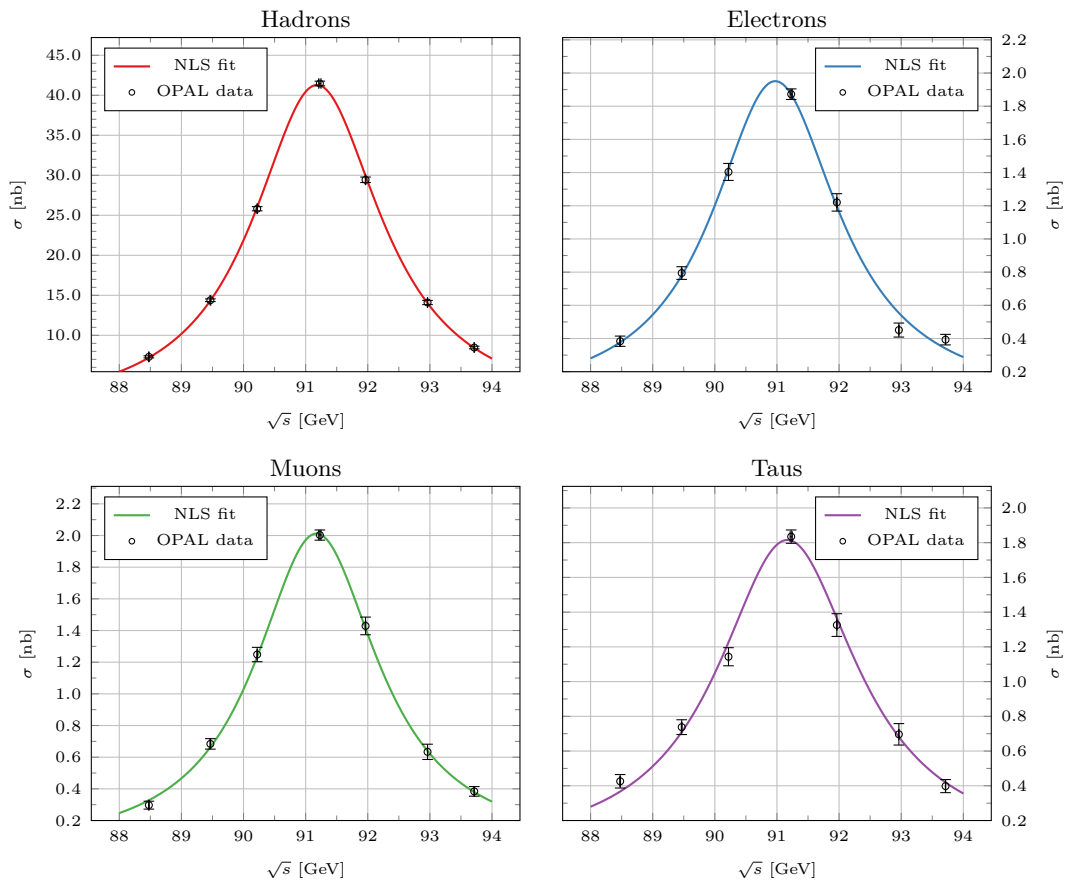


Figure 11: Cross sections of the different outgoing particle types at different beam energies. Note that error bars are plotted for both axes, even if the error in $\sqrt{s}$ is not visible.

Table 4: Fit results from the cross section fit displayed in fig. 11. The underlying model of the fit is a relativistic Breit-Wigner distribution given in eq. (43). As a measure for the goodness of fit, the residual standard error is given. For each of the fits, there are four degrees of freedom (df).

| Particle | $\Gamma_e\Gamma_f$ [$10^3$ MeV$^2$] | $M_{\rm Z}$ [GeV/$c^2$] | $\Gamma_{\rm Z}$ [GeV] | $\chi^2/$df |
|---|---|---|---|---|
| $e$ | 6.7± 0.5 | 90.99 ± 0.04 | 2.47± 0.11 | 1.53 |
| $\mu$ | 6.6± 0.2 | 91.19 ± 0.02 | 2.42± 0.04 | 0.73 |
| $\tau$ | 7.8± 0.6 | 91.19 ± 0.05 | 2.75± 0.12 | 1.26 |
| $h$ | 149.0± 1.7 | 91.198± 0.008 | 2.53± 0.02 | 1.02 |

Table 5: Overview over test statistics of the estimated parameters of each fit of table 4.

| Fit | $\Gamma_e\Gamma_f$ $t$-value | $\Gamma_e\Gamma_f$ $p$-value | $M_{\rm Z}$ $t$-value | $M_{\rm Z}$ $p$-value | $\Gamma_{\rm Z}$ $t$-value | $\Gamma_{\rm Z}$ $p$-value |
|---|---|---|---|---|---|---|
| $e$ | 13.55 | $1.72 \cdot 10^{-4}$ | 2103.15 | $3.07 \cdot 10^{-13}$ | 22.02 | $2.52 \cdot 10^{-5}$ |
| $\mu$ | 31.95 | $5.72 \cdot 10^{-6}$ | 4358.75 | $1.66 \cdot 10^{-14}$ | 54.84 | $6.62 \cdot 10^{-7}$ |
| $\tau$ | 13.81 | $1.59 \cdot 10^{-4}$ | 1863.73 | $4.97 \cdot 10^{-13}$ | 23.67 | $1.89 \cdot 10^{-5}$ |
| $h$ | 84.68 | $1.17 \cdot 10^{-7}$ | 11 247.12 | $3.75 \cdot 10^{-16}$ | −127.51 | $2.27 \cdot 10^{-8}$ |

### 3.3.2. Number of Neutrino Generations

Based on the fit results given in table 4 we are now able to calculate the partial width of each outgoing particle group we consider ($e, \mu, \tau$, and hadrons) and calculate their partial widths: To this end, we first consider the electron fit results and calculate the electronic decay width by taking the square root of $\Gamma_e\Gamma_f = \Gamma_e^2$. This gives

$$\Gamma_e = \sqrt{\Gamma_e^2} = (82 \pm 3)\,\text{MeV} \tag{44}$$

with the error propagated as

$$\sigma_{\Gamma_e} = \frac{1}{2\sqrt{\Gamma_e^2}}\sigma_{\Gamma_e^2} = 3.04\,\text{MeV}. \tag{45}$$

With the electronic decay width, we can calculate the remaining decay widths $\Gamma_f$ simply by dividing $\Gamma_e\Gamma_f$ by $\Gamma_e$. This gives

$$\begin{aligned}
\Gamma_\mu &= (82 \pm 3)\,\text{MeV}, \\
\Gamma_\tau &= (81 \pm 4)\,\text{MeV}, \\
\Gamma_\mu &= (1.81 \pm 0.07)\,\text{GeV},
\end{aligned} \tag{46}$$

where the error on the partial widths were propagated as

$$\sigma_{\Gamma_f} = \sqrt{\left(\frac{\sigma_{\Gamma_e \Gamma_f}}{\Gamma_e}\right)^2 + \left(\frac{\Gamma_e \Gamma_f}{\Gamma_e^2} \cdot \sigma_{\Gamma_e}\right)}, \qquad f \neq e. \tag{47}$$

Before we can calculate the invisible decay width and with that an estimate for the number of neutrino generations, we need a unique total decay width for the $Z^0$ boson. To this end we simply take the weighted mean of the values for $\Gamma_Z$ obtained via the fit and given in table 4:

$$\Gamma_Z = \frac{\sum_{f=e,\mu,\tau,h}(\Gamma_Z)_f \cdot \sigma_{(\Gamma_Z)_f}^{-2}}{\sum_{f=e,\mu,\tau,h} \sigma_{(\Gamma_Z)_f}^{-2}} = (2.54 \pm 0.07)\,\text{GeV}. \tag{48}$$

Here, $(\Gamma_Z)_f$ refers to the value for $\Gamma_Z$ obtained via the non-linear least squares fit over the cross sections of particle $f$. The error on the weighted mean was not propagated via normal error propagation. Instead, we opted for a more conservative estimation and used the standard deviation for a sample mean, i.e. we divided the sample standard deviation by $\sqrt{n} = \sqrt{4} = 2$ and used that as error for $\Gamma_Z$.

Now we are ready for the calculation of the invisible width, or rather, the number of neutrino generations: As presented in section 2.2, the neutrino decay width is given by $\Gamma_\nu = 165.88\,\text{MeV}$. Now, dividing the invisible width, which is the difference between the total decay width and the sum of the partial decay widths we observed, by the theoretical value for the neutrino decay width gives us the number of neutrino generations:

$$N_\nu = \frac{\Gamma_Z - \sum_{f=e,\mu,\tau,h}\Gamma_f}{\Gamma_\nu} = 2.6 \pm 0.6. \tag{49}$$

Again, the error was propagated using Gaussian error propagation:

$$\sigma_{N_\nu} = \frac{\sqrt{\sigma_{\Gamma_Z}^2 + \sum_{f=e,\mu,\tau,h}\sigma_{\Gamma_f}^2}}{\Gamma_\nu} = 0.615. \tag{50}$$

### 3.3.3. Lepton universality

Using the distribution of the cross section developed in section 3.3.1 we are ready to analyze lepton universality. As the cross section is proportional to the event rate, an interesting measure of the coupling between the $Z^0$ boson and leptons is given by the ratio $\sigma_f(M_Z)/\sigma_h(M_Z)$ $(f = e, \mu, \tau)$ right at the resonance. The calculation of $\sigma_f(M_Z)$ is straightforward; inserting $M_Z$ into the Breit-Wigner distribution gives

$$\sigma_f(M_Z) = \frac{12\pi \Gamma_e \Gamma_f}{M_Z^2 \cdot \Gamma_Z^2} \tag{51}$$

with error

$$\sigma_{\sigma_f(M_Z)} = \sqrt{\left(\frac{\partial \sigma_f}{\partial \Gamma_e \Gamma_f} \quad \frac{\partial \sigma_f}{\partial M_Z} \quad \frac{\partial \sigma_f}{\partial \Gamma_Z}\right) \cdot V_f \cdot \begin{pmatrix} \frac{\partial \sigma_f}{\partial \Gamma_e \Gamma_f} \\ \frac{\partial \sigma_f}{\partial M_Z} \\ \frac{\partial \sigma_f}{\partial \Gamma_Z} \end{pmatrix}}, \tag{52}$$

where $V_f$ is the covariance matrix of each fit. Table 6 shows the total cross section at the peak $\sigma_f(M_Z)$ as well as the ratio between the fermionic and the hadronic cross section at the peak. Further, the ratio between the partial decay widths are given. These were calculated using the results of the previous section and the error of this ratio was propagated by Gaussian error propagation,

$$\sigma_{\Gamma_f/\Gamma_h} = \sqrt{\left(\frac{\sigma_{\Gamma_f}}{\Gamma_h}\right)^2 + \left(\frac{\Gamma_f}{\Gamma_h^2}\cdot\sigma_{\Gamma_h}\right)^2}. \tag{53}$$

As one can see in table 6, the ratios of both the cross sections and the branching ratios are consistent in each respective group. In order to test if both ratios are in agreement (as predicted by eq. (51)), we can use a two-sample $t$-test on both ratios. A Welsh two sample $t$-test performed using `t.test` in R gives a $p$-value of 0.836; a two-sample Kolmogorov-Smirnov test using `ks.test` gives a $p$-value of 1. Though the significance of the Kolmogorov-Smirnov test can be disputed as it is an asymptotic test used on a sample of size 3, the Welsh two-sample test does not allow us to reject our hypothesis that both samples follow from the same distribution. Thus, our calculations seem consistent in itself.

Table 6: Total cross section at the $Z^0$ resonance for the different outgoing particles along with the ratio of the fermionic and hadronic peak cross section. Further, the ratio between the fermionic and hadronic partial decay widths are displayed.

| Particle | $\sigma_f(M_Z)$ [nb] | $\sigma_f(M_Z)/\sigma_h(M_Z)$ | $\Gamma_f/\Gamma_h$ |
|---|---|---|---|
| $e$ | $1.952\pm 0.018$ | $0.047 \pm 0.003$ | $0.045\pm 0.002$ |
| $\mu$ | $2.013\pm 0.003$ | $0.0488\pm 0.0016$ | $0.045\pm 0.003$ |
| $\tau$ | $1.815\pm 0.015$ | $0.044 \pm 0.003$ | $0.052\pm 0.004$ |
| $h$ | $41.3 \ \ \pm 0.3$ | $1$ | $1$ |

### 3.3.4. Forward-backward asymmetry

To calculate the forward-backward asymmetry $A_{\mathrm{FB}}$ of muons the Monte Carlo data for the muons must be separated into the events for which $0 < \cos\theta \leq 1$ holds and the ones where we have $-1 \leq \cos\theta < 0$. Note that this automatically removes the events for which the detector could not define a proper cosine. Further, this means that events with $\cos\theta = 0$ are not counted; however, we found none of such events. This selection by the value of $\cos\theta$ corresponds geometrically to picking the events with the outgoing particle in the forward and backward hemisphere with respect to the beam direction. After this separation by hemispheres, we count the number of muonic events in the forward region $N_{\mathrm{F}}$ and in the backward region $N_{\mathrm{B}}$ and calculate

$$A_{\mathrm{FB}} = \frac{N_{\mathrm{f}} - N_{\mathrm{b}}}{N_{\mathrm{f}} + N_{\mathrm{b}}} + \text{correction}, \tag{54}$$

"correction" is a beam-energy dependent correction term, which can be found in the appendix in table 9 and is responsible for the radiation corrections. Although this equation technically differs from eq. (9) in the theory as it would have to incorporate the cross sections and not just the number of events, but as the luminosity is the same for each cross section under consideration, the luminosity cancels out, so that one can calculate the forward-backward asymmetry directly from the event numbers $N_\text{f}$ and $N_\text{b}$. The error of $A_\text{FB}$ can be calculated as

$$\sigma_{A_\text{FB}} = A_\text{FB} \sqrt{\left( \frac{\sqrt{N_\text{f}}}{N_\text{f} + N_\text{b}} \right)^2 + \left( \frac{\sqrt{N_\text{b}}}{N_\text{f} + N_\text{b}} \right)^2 + \left( \frac{A_\text{FB}}{N_\text{f} + N\text{b}} \sqrt{N_\text{b}} \right)^2 + \left( \frac{A_\text{FB}}{N_\text{f} + N\text{b}} \sqrt{N_\text{f}} \right)^2}. \tag{55}$$

With the Monte Carlo data this results in

$$A_\text{FB}^\text{MC} = 0.022\,802 \pm 0.000\,015. \tag{56}$$

Under the assumption that the beam energy of the Monte Carlo events are close enough to the peak energy that eq. (15) can be used, the squared sine of the Weinberg angle $\sin^2 \theta_\text{W}$ can be calculated from the asymmetry with

$$\sin^2 \theta_\text{W} = \frac{1}{4} \cdot \left( 1 - \sqrt{\frac{A_\text{FB}}{3}} \right) \tag{57}$$

and propagate the error with

$$\sigma_{\sin^2 \theta_\text{W}} = \sin^2 \theta_\text{W} \frac{\sigma_{A_\text{FB}}}{8\sqrt{3 A_\text{FB}}}. \tag{58}$$

This gives us

$$\sin^2 \theta_\text{W} = 0.228\,294\,6 \pm 0.000\,001\,6. \tag{59}$$

Roughly the same calculations can be done for the real OPAL data. As before for the cross section calculation, the estimation for the real number of events can be calculated by multiplying the inverse of the efficiency matrix just as described in sections 2.4.1 and 3.3.1. The forward and backward number of events for each beam energy can be found in table 7. Forward-backward asymmetry and $\sin^2 \theta_\text{W}$ are calculated in the same way as for the Monte-Carlo data with the results shown in table 7. Furthermore the values for the forward-backward asymmetry $A_\text{FB}$ are plotted against the beam energies in fig. 12.

Having values for the forward-backward asymmetry at different beam energies allows us to refine our analysis a bit; before, we used eq. (57) for every value $A_\text{FB}$ regardless of the fact whether the beam energy is at resonance or not. Figure 12 shows the forward-backward asymmetry at different beam energies. By a Deming regression supplied by

the `R` package `deming` [9] we carry out a linear model of the form $A_{\mathrm{FB}} \sim \sqrt{s}$ with errors both in $A_{\mathrm{FB}}$ and in $\sqrt{s}$. The regression gives

$$\text{Intercept:} \quad -7.0 \pm 1.4, \tag{60}$$

$$\text{Slope:} \quad 0.077 \pm 0.015, \tag{61}$$

and as a prediction for $A_{\mathrm{FB}}(M_{\mathrm{Z}})$ at the resonance:

$$A_{\mathrm{FB}}(M_{\mathrm{Z}}) = 0.0046 \pm 0.0243 \quad \text{(rounding deliberately unorthodox)}. \tag{62}$$

The error was obtained by propagating the error of $M_{\mathrm{Z}} = (91.19 \pm 0.05)\,\mathrm{MeV/c^2}$ with covariance matrix given by the fit. The predicted value for the forward-backward asymmetry at the resonance is also depicted in fig. 12. Now, using this value we use the approximation given in eq. (57) applied to the newly obtained value and arrive at

$$\sin^2 \theta_{\mathrm{W}} = 0.239 \pm 0.005. \tag{63}$$

At this point we want to justify the choice of a linear model for the forward-backward asymmetry near the resonance. For one, the forward-backward asymmetry as a function of the center-of-mass energy is differentiable (for an analytic expression, see the reference [8]) and can thus be linearly approximated in a small neighbourhood. That this approximation is valid in the energy sector we consider can be seen by a visual inspection of the data points.

Table 7: Overview over the calculation of the forward backward asymmetry using OPAL data. Note that $\sin^2 \theta_{\mathrm{W}}$ is just an approximation and was calculated by using the (approximate) eq. (57).

| $\sqrt{s}$ [GeV] | $N_{\mathrm{f}}$ | $N_{\mathrm{b}}$ | $A_{\mathrm{FB}}$ | $\approx \sin^2 \theta_{\mathrm{W}}$ |
|---|---|---|---|---|
| $88.476 \pm 0.006$ | $35 \pm 6$ | $47 \pm 8$ | $-0.118 \pm 0.017$ | $0.2003 \pm 0.0007$ |
| $89.466 \pm 0.006$ | $103 \pm 11$ | $132 \pm 13$ | $-0.106 \pm 0.009$ | $0.2029 \pm 0.0004$ |
| $90.219 \pm 0.002$ | $209 \pm 15$ | $237 \pm 17$ | $-0.046 \pm 0.003$ | $0.2191 \pm 0.0002$ |
| $91.229 \pm 0.018$ | $1420 \pm 40$ | $1488 \pm 43$ | $-0.0057 \pm 0.0005$ | $0.239\,09 \pm 0.000\,11$ |
| $91.964 \pm 0.004$ | $290 \pm 20$ | $264 \pm 18$ | $0.084 \pm 0.003$ | $0.208\,10 \pm 0.000\,13$ |
| $92.9622 \pm 0.0014$ | $134 \pm 12$ | $68 \pm 9$ | $0.39 \pm 0.03$ | $0.1602 \pm 0.0005$ |
| $93.713 \pm 0.002$ | $148 \pm 13$ | $122 \pm 12$ | $0.191 \pm 0.007$ | $0.1869 \pm 0.0002$ |
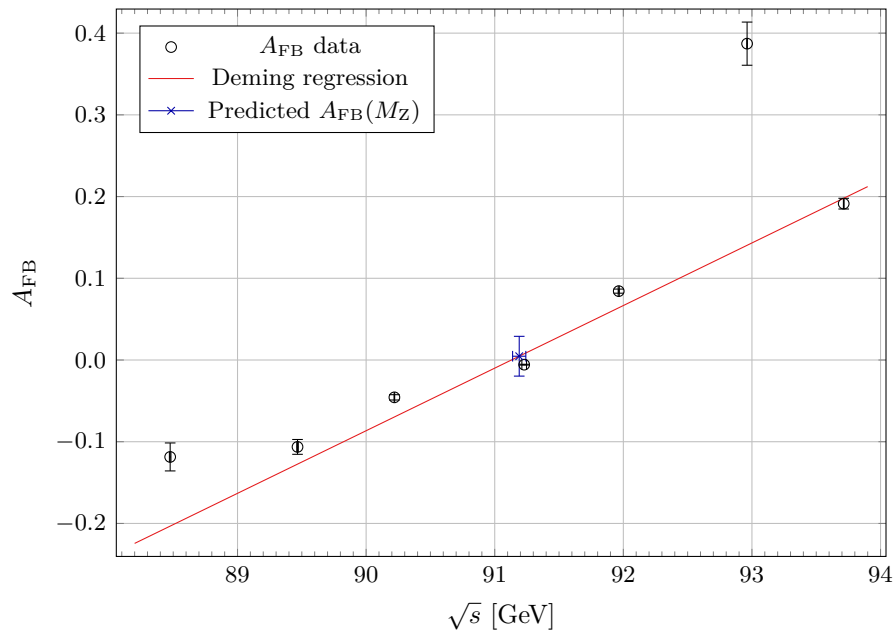
Figure 12: Forward backward asymmetry at different beam energies with linear deming regression and predicted $A_{\mathrm{FB}}$ value at the $\mathrm{Z}^0$ resonance.

# 4. Discussion

In the first part of the experiment GROPE was used to analyze example events using a graphical representation of the events in the detector. This provided a good opportunity to understand the meaning of the different measurement variables. Even if some ideas of cuts were made by using the GROPE example events the actual analysis started in the second part, when using the Monte-Carlo data. Using the histograms of the different measurement variables the cut finally were set as seen in table 8.

The hadron events and also the electron events could be cut out quiet nicely, but the separation of the muon and tau events turned out to be more difficult. As mentioned in the analysis (see section 3.2.1 and also in the theory in section 2.4) the muon events should show a high sum of momenta in the inner detector, which also is true for a lot of muon events but in the Monte-Carlo data there happens to be a peak not to be neglected at a zero momentum. One possible explanation for this peak could be that the momenta measurement at small angles is difficult and the actual momentum can not be measured. This explanation is supported by the fact that the muon events with a zero momentum do have a small or non defined angle, but it is puzzling that the number of charged tracks was correctly detected to be two most of the time regardless of which momentum was measured. This deviation from expectations may could be interesting to look at more closely, but this would need to have accessibility to the code which provides the Monte Carlo data. Over all regarding the cuts one can say that the analysis done to define the cuts is highly simplistic and the actual analysis done at OPAL [1] goes a lot more into detail, but such a intense analysis would easily exceed the time frame of this lab course. So, while it certainly is comfortable working with data that we got as tidy data (i. e. a model matrix) it would certainly be interesting from the physical point of view to learn more about the way the "raw" detector data gets to that tidy form.

Using the OPAL data we could obtain four different values for the $Z^0$ mass from the Breit-Wigner fits, calculating the mean for the four masses gives us the result

$$M_{\mathrm{Z}} = (91.19 \pm 0.05)\,\mathrm{GeV}. \tag{64}$$

In comparison the value for 2020 given by the Particle Data group [4]

$$(91.1876 \pm 0.0021)\,\mathrm{GeV}. \tag{65}$$

| Condition | Particle assignment |
|---|---|
| N.CHARGED $\geq 7$ | Hadron |
| E.ECAL $< 25$ and (P.CHARGED $\geq 70$ or P.CHARGED $= 0$) | Muon |
| E.ECAL $\geq 70$ | Electron |
| E.ECAL $< 70$ and $0 <$ P.CHARGED $< 70$ | Tau |

Table 8: Final cut values used to separate events and assign them outgoing particles. The conditions are hierarchically ordered, that is, an event only passes a condition if it hasn't passed the conditions above that one before. Events without particle assignment get discarded.

## 4. Discussion

This reference value lies in a 1-$\sigma$ environment of our result (with respect to our error) while having a relative error of just $\approx 0.05\,\%$. All in all, this result can be considered quite good.

Further, the full decay width of the $Z^0$ boson was obtained in the form of four different values – one from each fit – and the mean was calculated to be

$$\Gamma = (2.52 \pm 0.07)\,\text{GeV}. \tag{66}$$

In comparison, the value given by the Particle Data group [4] is

$$(2.4952 \pm 0.0023)\,\text{GeV}. \tag{67}$$

Again, the reference value lies in a 1-$\sigma$ environment while this time the relative error being about $3\,\%$, so the result is again compatible with the reference value. This time, however, the precision of the result is by far not as good as for the mass of the $Z^0$ boson as can be seen in the paragraph above.

Also the partial decay widths into each of the four considered groups of outgoing particles could be calculated using the fits:

$$\Gamma_e = (82 \pm 3)\,\text{MeV}, \tag{68}$$
$$\Gamma_\mu = (81 \pm 4)\,\text{MeV}, \tag{69}$$
$$\Gamma_\tau = (85 \pm 8)\,\text{MeV}, \tag{70}$$
$$\Gamma_h = (1820 \pm 70)\,\text{MeV}. \tag{71}$$

Again this values can be compared to the once given by the Particle Data Group, which is

$$(83.984 \pm 0.086)\,\text{MeV} \tag{72}$$

in the case of leptons and in the hadronic case

$$(1744.4 \pm 2.0)\,\text{MeV}. \tag{73}$$

So for the leptons the reference value again lays in a 1-$\sigma$ environment for each three values we have, with the result for tau being the least precise with a relative error of approximately $9\,\%$ and the electrons giving the most precise lepton result with a relative error of approximately $4\,\%$. The hadron decay width given by the dpg lays in a 2-$\sigma$ environment of our result, while the result has an relative error of about $4\,\%$.

The quality of the results may be surprising, considering the small number of data points for each fit, leaving just four degrees of freedom: We did fit Breit-Wigner functions with three fit parameters to seven data points which is not too satisfying. One way to obtain results with a higher precision would probably be to use data sets where the beam energies are spread out more. Of course, this would also entail having the knowledge of the luminosity of these beam events.

## 4. Discussion

Using our results and the theoretical value for the neutrino decay width we could calculate the number of neutrino generation which resulted in

$$N_\nu = 2.7 \pm 0.6. \tag{74}$$

The Particle Data Group gives as number of neutrino generation determined by measurement of the invisible $Z^0$ width

$$2.92 \pm 0.05. \tag{75}$$

So our result is compatible with this reference value and also compatible with the expected value of three, but it is rather inaccurate with an relative error of $\approx 20\,\%$.

To verify the lepton universality, the branching ratio for the three different lepton events was calculated:

$$\frac{\Gamma_e}{\Gamma_h} = 0.045 \pm 0.002, \tag{76}$$

$$\frac{\Gamma_\mu}{\Gamma_h} = 0.045 \pm 0.003, \tag{77}$$

$$\frac{\Gamma_\tau}{\Gamma_h} = 0.052 \pm 0.004. \tag{78}$$

While the branching ratio for the electrons and the muons are well compatible with each other, the tau branching ratio varies the other two. This variation is not to bad and this ratios still assist the assumption of a lepton universality. It is also not too surprising that we get the most divergent results for the tau, since our cuts were the less efficient for the tau events. Choosing the tau events to be the least efficient particles was almost as deliberate choice: in setting the cuts we had to balance the background and asymptotic loss of each particle type. In order to make our electron and muon cuts more pure (the hadronic events didn't matter at this point, because they were quite easily dealt with using the N.CHARGED cut), we had to sacrifice the "purity" of the tau events. The reason we wanted the electron and muon events to be the most efficient is twofold: First, the calculation of each partial decay relies on knowing the electronic decay width. Making this decay width the most accurate by selecting electrons to be extremely clean seems like a reasonable choice. Second, only the muonic events are used for the calculation of the forward-backward asymmetry and thus the electro-weak mixing Angle $\theta_\text{W}$. Because of these reasons, we deemed the tau events to of least importance for the analysis.

The last analysis done in this report was the calculation of the forward-backward asymmetry and using this the squared sine of the Weinberg angle $\sin^2\theta_\text{W}$. From the Monte Carlo data the forward-backward asymmetry was calculated to be

$$A_\text{FB}^\text{MC} = 0.022\,802 \pm 0.000\,015. \tag{79}$$

and, assuming that the beam energy used for the Monte-Carlo data is near the peak energy, the squared sine of the Weinberg angle was estimated as

$$\left(\sin^2\theta_\text{W}\right)_\text{MC} = 0.228\,294\,6 \pm 0.000\,001\,6. \tag{80}$$

## 4. Discussion

The results of the same calculations for the OPAL data can be found in table 7. Since the formula used for the calculation of the squared sin of the Weinberg angle is an approximation only valid at the resonance peak of $Z^0$ we did an additional calculation of the squared sine of the Weinberg angle. We carried out a linear model of the form $A_{\mathrm{FB}} \sim \sqrt{s}$ and, using this linear model, predicted the forward-backward asymmetry at the resonance to be

$$A_{\mathrm{FB}}(M_{\mathrm{Z}}) = 0.0046 \pm 0.0243. \tag{81}$$

From this we obtained the final result

$$\sin^2 \theta_{\mathrm{W}} = 0.239 \pm 0.005. \tag{82}$$

As before we use the Particle Data Group for the reference value which is

$$0.231\,21 \pm 0.000\,04. \tag{83}$$

So the reference value lays in a 2-$\sigma$ environment of our result obtained by the linear model. Keeping in mind that we could only use seven different data points for the linear model and the model itself is just an approximation this result seems to be quite good. Looking at table 7 and the result for the Monte-Carlo data one can find that the approximation in eq. (57) seems to be decent if the beam energy is close to the resonance peak.

# List of Figures

## List of Tables

## References

[1] ALEPH Collaboration, DELPHI Collaboration, L3 Collaboration, OPAL Collaboration, SLD Collaboration, LEP Electroweak Working Group, SLD electroweak, heavy flavour groups. *Physics Reports* 427.5-6 (2006), pp. 257–454. DOI: 10.1016/j.physrep.2005.12.006.

# References

[2] Jonathan P. Couchman. *A Measurement of the Triple Gauge Boson Couplings and W Boson Polarisation in W-Pair Production at LEP2*. 2000. URL: http://www.hep.ucl.ac.uk/~jpc/all/ulthesis/ulthesis.html.

[3] Jones; Eric, Travis Oliphant, Pearu Peterson, et al. *SciPy: Open source scientific tools for Python*. Online; Accessed on Aril 2nd, 2021. 2001–. URL: https://www.scipy.org/.

[4] Particle Data Group et al. "Review of Particle Physics." *Progress of Theoretical and Experimental Physics* 2020.8 (2020). 083C01. DOI: 10.1093/ptep/ptaa104.

[5] M. Lefebvre et al. "Propagation of errors for matrix inversion." *Nuclear Instruments and Methods in Physics Research Section A: Accelerators, Spectrometers, Detectors and Associated Equipment* 451.2 (2000), pp. 520–528. DOI: 10.1016/s0168-9002(00)00323-5. arXiv: 9909031 [physics.hep-ex].

[6] Bogdan Povh et al. *Teilchen und Kerne*. Physics and astronomy online library. Springer Berlin Heidelberg, 2014.

[7] R Core Team. *R: A Language and Environment for Statistical Computing*. R Foundation for Statistical Computing. Vienna, Austria, 2021.

[8] S. A. *Analyse von $Z^0$-Zerfällen*. 1995.

[9] Terry Therneau. *deming: Deming, Theil-Sen, Passing-Bablock and Total Least Squares Regression*. R package version 1.4. 2018. URL: https://CRAN.R-project.org/package=deming.

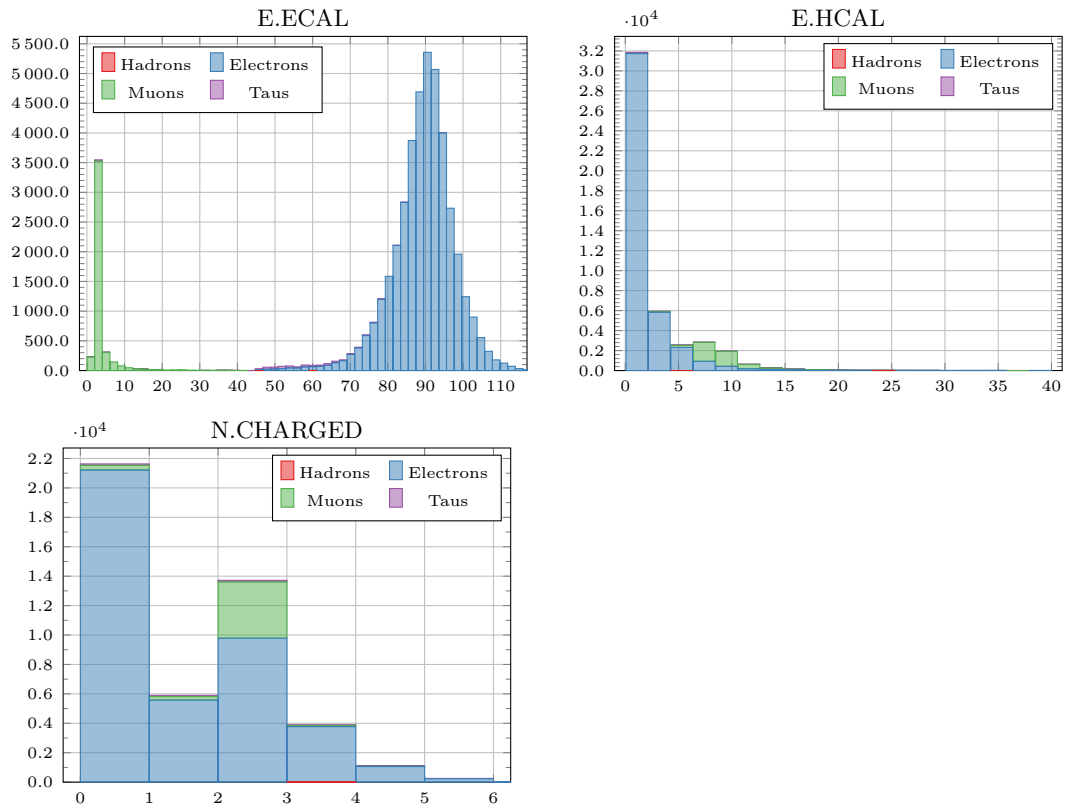[10] D. Ward and J. Banks. "A GRope Primer." *OPAL internal note* GR202 (1995).

# A. Appendix



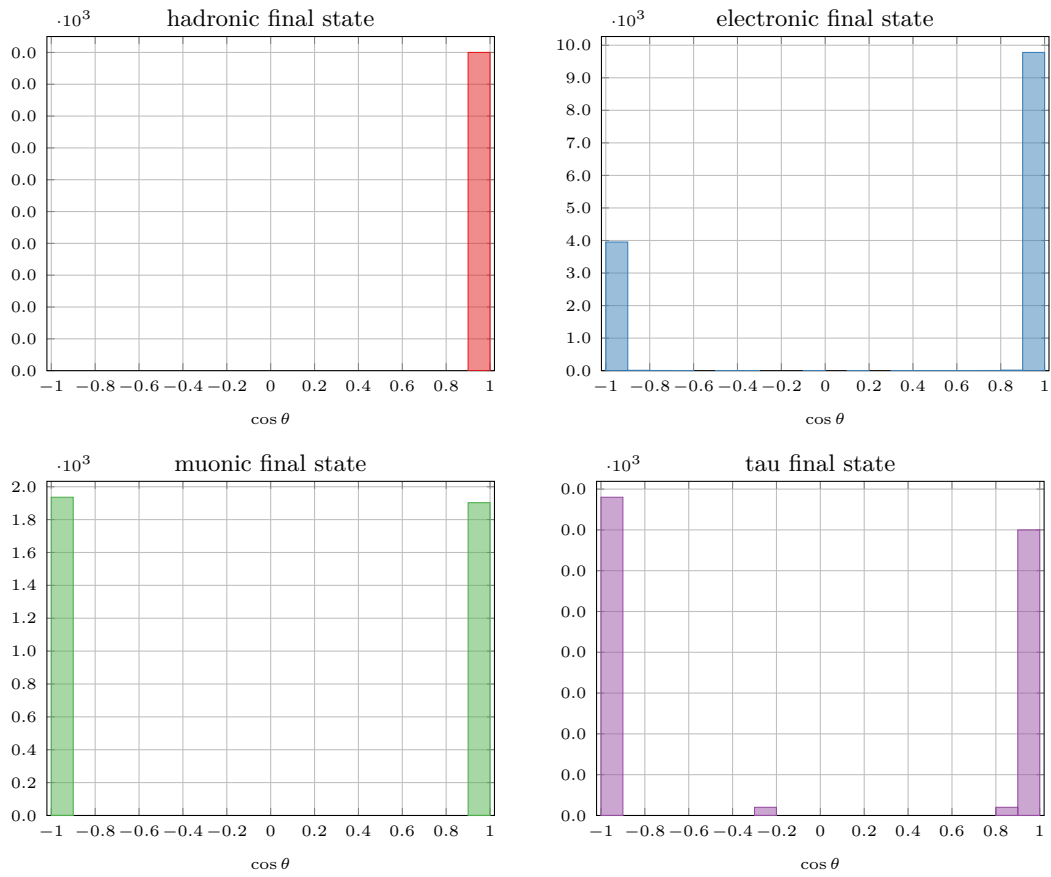Figure 13: Histograms for the different measurement variables in the Monte-Carlo data set for which P.CHARGED vanishes.

Figure 14: Histograms for angular distribution of the particles in the Monte-Carlo data set for which P.CHARGED vanishes.
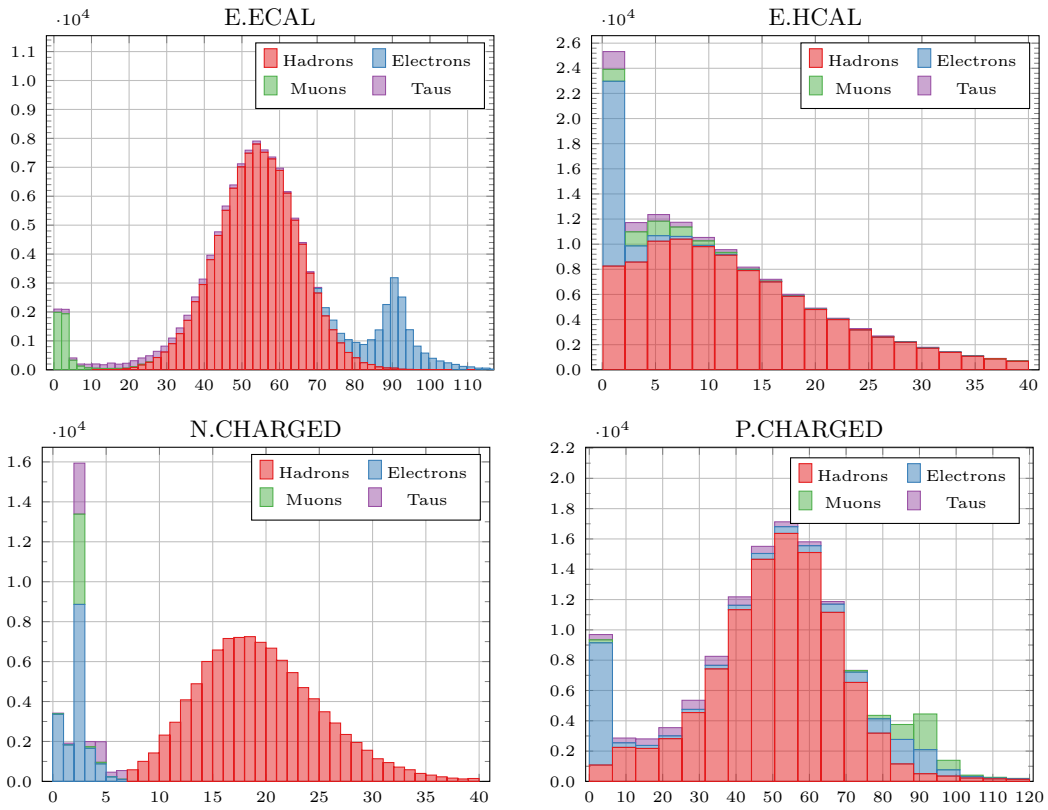
Figure 15: Histograms for the different measurement variables in the OPAL data set. Note that the particle types given here are only the one assigned by our selection scheme.
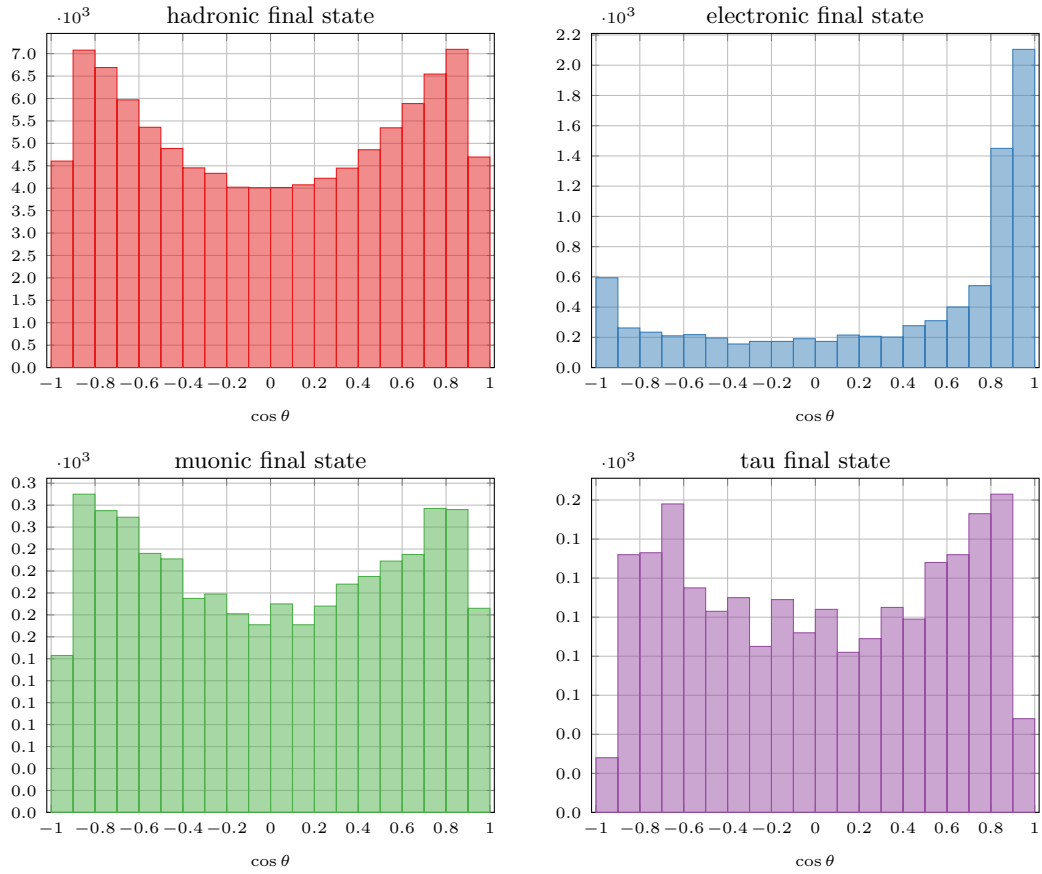
Figure 16: Histograms for the angular distribution of the events in the OPAL data set. Note that the particle types given here are only the one assigned by our selection scheme.

Table 9: Radiation corrections to the cross section and to the forward backward asymmetry for a specific beam energy.

| $\sqrt{s}$ [GeV] | Correction to $\sigma$ | | Correction to $A_{\mathrm{FB}}$ |
|---|---|---|---|
| | Hadronic channel | Leptonic channel | |
| 88.47 | 2.0 | 0.09 | 0.021 512 |
| 89.46 | 4.3 | 0.20 | 0.019 262 |
| 90.22 | 7.7 | 0.36 | 0.016 713 |
| 91.22 | 10.8 | 0.52 | 0.018 293 |
| 91.97 | 4.7 | 0.22 | 0.030 286 |
| 92.96 | −0.2 | −0.01 | 0.062 196 |
| 93.76 | −1.6 | −0.08 | 0.093 850 |